Principles and applications of EPR spectroscopy in the chemical sciences

(Article begins on next page)

Principles and Applications of EPR Spectroscopy in the Chemical Sciences

Maxie M. Roessler[a,b,*] and Enrico Salvadori[a,b,*]

[a] School of Biological and Chemical Sciences and [b] Materials Research Institute, Queen Mary University of London, Mile End Road, London, E1 4NS, United Kingdom

[*] Corresponding authors. E-mail: m.roessler@qmul.ac.uk, e.salvadori@qmul.ac.uk

ABSTRACT

Electron spins permeate every aspect of science and influence numerous chemical processes: they underpin transition metal chemistry and biochemistry, mediate photosynthesis and photovoltaics and are paramount in the field of quantum information, to name but a few. Electron Paramagnetic Resonance (EPR) spectroscopy detects unpaired electrons and provides detailed information on structure and bonding of paramagnetic species. In this tutorial review, aimed at non-specialists, we provide a theoretical framework and examples to illustrate the vast scope of the technique in chemical research. Case studies were chosen to exemplify systematically the different interactions that characterize a paramagnetic centre and to illustrate how EPR spectroscopy may be used to derive chemical information.

Key learning points

1. An understanding of the physical principles in EPR spectroscopy is fundamental to deriving any information from EPR spectra beyond simple detection of the signals.

2. EPR spectroscopy can tackle many different chemical questions, ranging from identification of the paramagnetic centre, to detailed information on structure and bonding.

3. Many continuous-wave and pulse EPR experiments exist. Pulse EPR experiments are frequently designed to single out a particular magnetic interaction (e.g. hyperfine coupling, dipolar coupling) and choosing the right experiment is often key to success.

4. Visual inspection of EPR spectra may lead to good estimates of parameters (e.g. g values, hyperfine coupling constants or even zero-field splitting), but simulation is usually required to interpret spectra fully.

1   Introduction

Since Yevgeny Zavoisky recorded the first EPR spectra of copper and manganese over 70 years ago on a home-built spectrometer, EPR spectroscopy has made seminal contributions in all areas of chemistry, as well as in biology, physics and materials science. However, to many chemists EPR spectroscopy is not a very accessible field. This is perhaps because most EPR literature is aimed at experienced researchers already working in the field. A few introductory textbooks[1–3] provide an excellent and thorough bottom-up approach for new researchers entering the field of EPR spectroscopy, but are not designed to provide a short general overview with a wide range of examples. There are however several accessible reviews on specialised topics that the interested reader is referred to: e.g. metallobiomolecules,[4] in-situ EPR (heterogeneous catalysis),[5] and ENDOR.[6] Here, we aim to close the gap between EPR spectroscopists and chemists not acquainted with EPR, with a tutorial review that provides a basic theoretical background, introduces a representative range of current EPR methods and provides an illustration of the chemical questions that may be answered using this lesser-known and advancing magnetic resonance spectroscopy method.

1.1   EPR versus NMR

NMR spectroscopy (discovered just a year after Zavoisky's EPR experiments) and EPR share the same fundamental principles and it is useful to begin by comparing these two magnetic resonance spectroscopies (Table 1).

Table 1. Comparison between NMR and EPR. Note that for simplicity some generalisations were made: e.g. the resonance frequency.[1]

	NMR	EPR
Spin under investigation	nuclear spins	electron spins
	often many per molecule	often just one per molecule
Spin quantum number	$I \geq 1/2$	$S \geq 1/2$
Magnetic quantum number	$m_I = \pm1/2, \pm1, \pm3/2, \ldots$	$m_S = \pm1/2, \pm1, \pm3/2, \ldots$

---

[1] Table adapted from third-year physical chemistry lectures notes (2005) by Professor Peter Hore (University of Oxford).

Characteristic property	chemical shift	g values
Resonance frequency	MHz	GHz
Sensitivity	mM concentrations required	µM concentrations required
Relaxation times	~s	~µs
Linewidths (~1/relaxation time)	Hz	MHz
Time resolution	~ms	~ns

Both EPR and NMR probe the interaction of magnetic dipoles with an applied magnetic field and electromagnetic radiation of the appropriate wavelength. Whilst NMR is concerned with the splitting of nuclear spin states in a magnetic field, EPR is concerned with the splitting of electronic spin states. A nuclear magnetic dipole arises from the combined spin of neutrons and protons in a nucleus, whereas an electron magnetic dipole arises from one or more unpaired electrons. However, while most compounds have at least one NMR-active nucleus (i.e. $I \geq 1/2$), usually protons, not all molecules are "EPR active" because most stable molecules have a closed electronic shell. Indeed, EPR spectroscopy often involves just a single unpaired electron ($S = 1/2$). The presence of multiple unpaired electrons ($S > 1/2$) is common in e.g. transition metals and can result in EPR spectra that are much more difficult to interpret (Section 5). A much higher frequency of electromagnetic radiation is required for EPR (microwaves) compared to NMR (radiowaves), and EPR is approximately three orders of magnitude more sensitive than NMR. Consequently, magnetic field strengths are usually much lower in EPR and measurements are typically recorded using electro- rather than superconducting magnets. The most common 'X-band' EPR uses a microwave frequency of ~ 9.5 GHz and an applied field of ~ 0.3 T. The sensitivity limit in EPR is approximately 10^{13} spins, but this value should only be taken as a very approximate reference point because it is hugely dependent on the width of the EPR spectrum (anisotropy, see Section 2.1), the spin system (high spin states with $S > ½$ typically require higher spin concentrations) and experimental conditions. The much faster relaxation times (Section 2.8) in EPR have two immediate consequences: unlike NMR, the sample often has to be frozen to enable observation of a spectrum, and lines in EPR spectra are much broader.

1.2   The scope of EPR and of this review

Given the requirement for at least one unpaired electron, one may conclude that few compounds are amenable to EPR spectroscopy. Fortunately, this is not the case since many diamagnetic compounds can be spin labelled, or cycle through functional states that are paramagnetic and that can be obtained through reduction, oxidation, photoexcitation, or trapped using rapid freeze-quench. In this review, we cannot do justice to all the different research areas where EPR spectroscopy is applied, and we do not discuss the instrumental and experimental developments in the field. Rather, we have attempted to choose examples that illustrate the principles we introduce in an accessible manner. Moreover, given the wide scope of EPR spectroscopy, we cannot provide a complete overview of all its applications and we focus on areas that are arguably most relevant to the chemical sciences (green ovals in Figure 1).
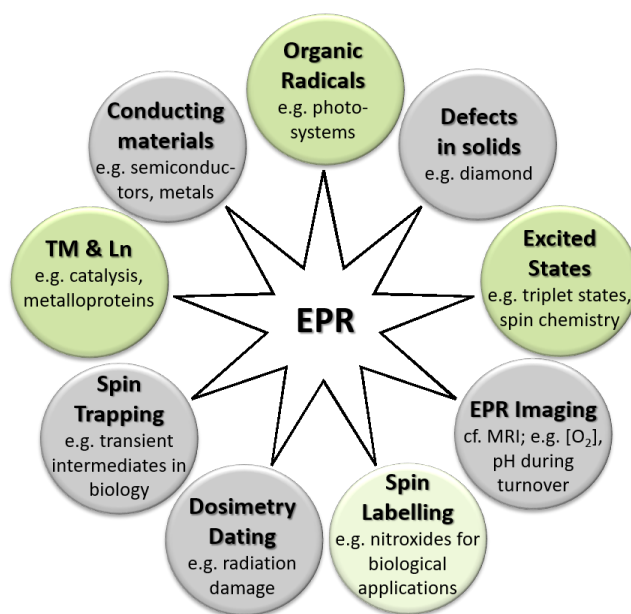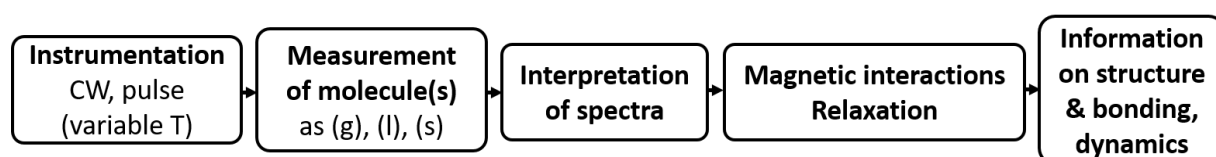
Figure 1. Scope of EPR spectroscopy and this Tutorial Review. Green circles represent topics that are discussed in some detail; spin-labelling (light green) is only discussed peripherally and grey circles represent topics (e.g. spin trapping in biology,[7] EPR imaging in cardiology,[8] defects in diamond,[9] dosimetry applied to teeth[10]) that are not discussed here. Abbreviations: TM = transition metals, Ln = lanthanides.

A major and perhaps obvious advantage of EPR spectroscopy stems from the fact that the technique is blind to the many paired electrons in a molecule. Thus, information specifically about the centre with unpaired electron(s) and its interaction with the environment can be obtained. The information that EPR can provide on the structure and dynamics of (bio)chemical

systems is heavily reliant on choosing the 'right' EPR experiments and on spectral interpretation (Scheme 1). This is turn requires a solid understanding of the magnetic interactions at play. A discussion of the fundamental physical principles behind EPR spectroscopy (Section 2) will provide a framework for the subsequent sections of this review, that present examples falling into the different areas in Figure 1 (green circles). Indeed, such a foundation is required in order to illustrate what EPR can measure and what information can be gained – and thus what chemical questions may be answered.

Instrumentation CW, pulse (variable T)	Measurement of molecule(s) as (g), (l), (s)	Interpretation of spectra	Magnetic interactions Relaxation	Information on structure & bonding, dynamics

Scheme 1. Flow of measurements and information in EPR. Abbreviations are as follows: T = temperature, g = gas, l = liquid, s = solid; e⁻ = electron. For the different magnetic interactions see Section 2. Note that the application of EPR to liquid or solid samples prevails and gaseous example are not discussed in this review.

2   Fundamental Physical Principles

The fundamental principles presented in this section are necessarily in abridged form. For accessible introductory textbooks, the reader is referred to the book edited by Brustolon and Giamello (offering a practical approach),[3] the recently published EPR Oxford Chemistry Primer (offering an excellent treatment of fluid solutions in particular)[1] and the book by Hagen (focussing on biological EPR)[2]. A more advanced account can be found in Weil and Bolton,[11] and the

Box 1: Calculating energy levels

The spin Hamiltonian (H_0) enables calculations of the energy levels of the spin system. For a system with a single electron (or multiple strongly-coupled electrons in a single paramagnetic centre) and l nuclear spins H_0 is given by:

$$H_0 = H_{EZ} + H_{NZ} + H_{HF} + H_{NQ} + H_{NN} + H_{ZFS} \qquad (1a)$$

$$H_0 = \beta_e \mathbf{B_0 g S}/\hbar - \beta_n \sum_{k=1}^{l} g_{n,k} \mathbf{B_0 I_k}/\hbar + \sum_{k=1}^{l} \mathbf{S A_k I_k} + \sum_{I_k > \frac{1}{2}} \mathbf{I_k Q_k I_k} + \sum_{i \neq k} \mathbf{I_i d_{ik} I_k} + \mathbf{S D S} \qquad (1b)$$

where the six energy terms (given in angular frequency units here) describe the electron Zeeman, nuclear Zeeman, hyperfine, nuclear quadrupole, nuclear-nuclear and the zero-field splitting interactions, that are explained in Sections 2.1 to 2.7. In equation 1b, variables are in italics, vectors and matrices are in bold, β_e is the Bohr magneton and β_n is the nuclear magneton. $\mathbf{S}$ (the electron spin operator with electron-spin quantum number $S = n/2$, where n is the number of unpaired electrons) is analogous to $\mathbf{I}$ (the nuclear spin operator with nuclear-spin quantum I that depends on the nucleus) in NMR.

If more than one non-interacting paramagnetic centre is present, each centre is characterised by its own spin Hamiltonian. For interacting paramagnets (e.g. many dimers or diradicals) additional coupling terms have to be included.

book by Schweiger and Jeschke[12] is considered to be the reference work for pulsed EPR principles and spectral interpretation. For experimental aspects of EPR, the reader is referred to Poole.[13] In addition, the 2017 volume of the online book *eMagRes*[14] covers every aspect of modern EPR spectroscopy from instrumentation and methodology to applications in detail.

Here, we have taken a qualitative approach to introduce the fundamental physical principals. The more quantitatively-oriented reader is referred to the text boxes that supplement the text. In order to understand the structure and bonding of a paramagnetic system, we need to understand the different magnetic interactions present as these determine the spacing between energy levels (Box 1). From the transitions between these magnetic energy levels (measured experimentally) energies can be derived and used to deduce information on structure and bonding. In the following sections, we introduce the different types of magnetic interactions. Note that not all of these interactions are necessarily present in any one spin system.

2.1   *The Electron Zeeman Interaction* (H_{EZ})

This fundamental interaction between the unpaired electron(s) and the applied magnetic field is described by g *values that are analogous to the chemical shift in NMR.*

The g value can thus be used as an identifier for a given paramagnetic species. Since the unpaired electron is typically bound to a molecule, the g value for a given paramagnet usually deviates from g_e (the free-electron g value, $\sim$ 2.0023). The magnitude of the shift depends on the molecular environment and ultimately the spin-orbit interaction (that scales with atomic number); it is small for organic radicals ($g \sim 2$) and can be very large in transition metal or lanthanide complexes. Similar to the chemical shift in NMR, g values are independent of the operating frequency of the instrument. In EPR, the operating frequency, that goes hand in hand with the applied magnetic field strength, refers to the frequency of the microwave radiation of the source. Note that g values designate the intrinsic resonance position of a radical in a particular environment rather than being given relative to a reference compound (like in NMR).

2.1.1 Solid state – anisotropy

Unlike in NMR, in EPR spectroscopy we frequently work in the solid state, i.e. with powders or frozen solutions. Thus, whereas in solution molecular tumbling leads to a measured averaged g, in the solid state g has three components ($g_1, g_2, g_3,$ or g_x, g_y, g_z, if the g values have been assigned to the Cartesian axes) that depend on the orientation of the molecule with respect to the applied magnetic field. This anisotropy of the electron Zeeman interaction gives a measure of the

> **Box 2: g values**
>
> **g** is a 3x3 matrix (equation 1b) that can be diagonalised to yield three principal components (g_x, g_y, g_z) as well as three Euler angles that describe the orientation of this tensor in a given molecular frame.
>
> Since $\Delta E = g\beta_e B_0$ (see Figure 2) and given that the EPR spectrometer operates at fixed frequency so that ΔE is a constant, B_0 and g are inversely proportional: as the g value decreases the corresponding resonant field increases and vice versa.

symmetry of the electronic distribution within the paramagnetic species. Therefore, depending on the symmetry of the electronic distribution, g can be isotropic ($g_x = g_y = g_z = g_{iso}$, cubic symmetry, e.g. a metal with six identical ligands in a perfectly octahedral environment), axial ($g_x = g_y \neq g_z$, where $g_\perp$ is often used for $g_x = g_y$ and $g_{||}$ for g_z) or rhombic ($g_x \neq g_y \neq g_z$), as illustrated in Figure 2A. The g value measured in solution is the average of the three components and it is also referred to as the g_{iso} (see Figure 2A).
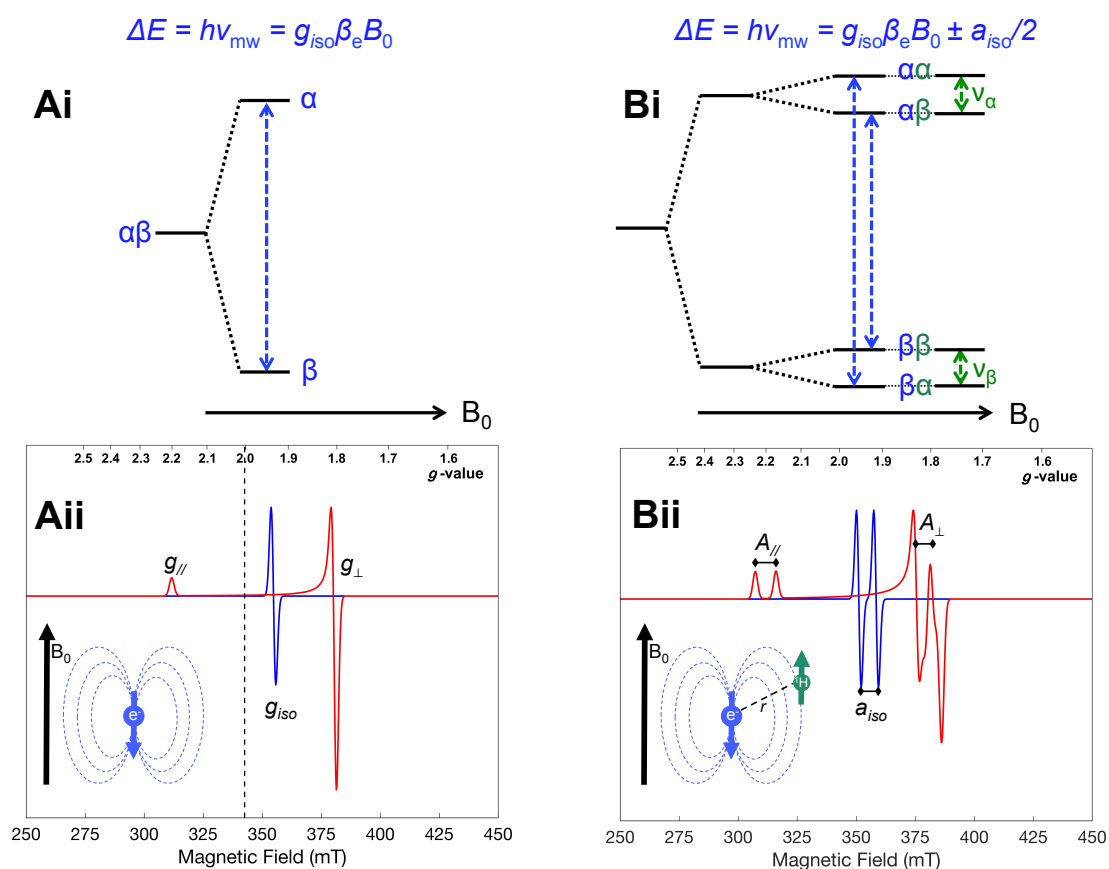
Figure 2. Energy level diagrams, transitions and field-swept EPR spectra to illustrate the (A) Zeeman interaction (EZ) for a system with a single unpaired electron ($S = \frac{1}{2}$) and (B) hyperfine interaction (HF) with a $I = \frac{1}{2}$ nucleus (e.g. ^{1}H). HF transitions are governed by the selection rules Δm_s = ± 1 (where m_s = +1/2 = α, m_s = −1/2 = β, blue labels) and $\Delta m_I = 0$ (where m_I = +1/2 = α, m_I = −1/2 = β, green labels). In both Ai and Bi EPR transitions (blue doted arrows) are only shown for the isotropic case, giving rise to lines in the corresponding blue CW EPR spectra shown in Aii and Bii. In Bi, the NMR transitions (nuclear transition frequencies) in the α and β electron-spin manifolds are denoted with ν_α and ν_β, respectively. The dotted line in Aii marks the resonance position for a free electron at g = 2.0023. The equations describing the resonance conditions in each case are given above the corresponding energy level diagram (ν_{mw} = applied microwave frequency). The insets in Aii and Bii depict the magnetic interactions at play. Note that g_{iso} (taken arbitrarily as g = 1.93) is the average of $2g_\perp$ (1.80) and $g_{||}$ (2.20); similarly, a_{iso} (130 MHz) is the average of $2A_\perp$ (60 MHz) and $A_{||}$ (270 MHz). CW spectra were simulated using EasySpin (microwave frequency 9.6 GHz, linewidth 2 mT).

The electron Zeeman interaction depends on the applied magnetic field (see equation 1b in Box 1). As we shall see in Section 3.1, this field dependence can be exploited when dealing with complex spectra given that, similar to NMR, recording EPR spectra at different magnetic fields allows the separation of field-dependent and field-independent interactions.

8

2.2 *The Nuclear Zeeman Interaction* (H$_{NZ}$)

This interaction between the nuclear spin(s) and the applied magnetic field is analogous to the electron Zeeman interaction but usually only needs to be considered in pulsed EPR.

Given that each nucleus interacts differently with the applied magnetic field, the nuclear Zeeman interaction plays a major role in NMR spectroscopy. The NZ interaction has little effect in CW-EPR spectra (see Box 3), but is significant in pulse EPR.

2.3 *The Electron-Nuclear Hyperfine Interaction* (H$_{HF}$)

This interaction between the magnetic dipoles of unpaired electrons and surrounding nuclei (typically within 5 Å, e.g. ^1H, ^{13}C, ^{14}N, ^{31}P, ^{51}V, $^{63,65}Cu$) is perhaps the most important source of chemical information in EPR.

> **Box 3: Nuclear *g* values**
>
> Protons have the largest nuclear *g* value (g_n) of all nuclei, yet their nuclear Zeeman interaction is only 1/658 of the electron Zeeman interaction because of the much smaller mass of the electron ($\beta_e = \frac{e\hbar}{2m_e}$ and $\beta_n = \frac{e_p\hbar}{2m_p}$, where m_p and e_p are the proton mass and charge, respectively). Using $\Delta E_{EPR} = g\beta_e B_0$ and $\Delta E_{NMR} = g_n\beta_n B_0$, this explains why EPR spectroscopy requires lower magnetic fields and higher frequencies than NMR.
>
> In field-swept EPR spectra (Section 2.9), transitions between nuclear sublevels are forbidden by the selection rules ($\Delta m_S = \pm 1$, $\Delta m_I = 0$), see Figure 2.

The hyperfine interaction (A) consists of two contributions: the isotropic and anisotropic parts. The isotropic part (a_{iso}) is a through-bond interaction and is related to the probability of finding the electron spins at the position of the nucleus, i.e. the occupied orbital must have some *s*-orbital character (Box 4). It is noteworthy that isotropic contributions are routinely measured in metals or radicals where the unpaired spin is nominally in *p* orbitals (π radicals, e.g. pentacene radical anion/cation) or *d* and *f* orbitals (transition metals and lanthanides). This is because there are mechanisms that transfer (polarise) the spin orientation of the unpaired electron in the *p,d,f* orbitals to the inner *s* orbitals. Knowledge of a_{iso} thus allows the mapping of spin delocalisation onto molecular structure, providing information on the nature and spatial extent of the orbital in which the unpaired electron resides.

The anisotropic part (T) is a pure magnetic dipole – dipole interaction that averages out in liquid solution and is thus only be detected in the solid state. T depends on the orientation and the average distance between the unpaired electron and the magnetically active nucleus. Like g in the solid state, T has three components (T_x, T_y, T_z, along each Cartesian axis). In EPR, particularly in solids, T can be used to derive spatial information. Hyperfine EPR spectroscopy has been used to obtain functional information on specific magnetic nuclei, for instance protons that are often ill-defined in structures

> **Box 4: A more quantitative look at the hyperfine interaction.**
>
> For an electron coupled to a single nuclear spin, the hyperfine Hamiltonian is given by:
>
> $$H_{HF} = \mathbf{SAI}. \qquad (2)$$
>
> The hyperfine matrix $\mathbf{A}$ consists of an isotropic and an anisotropic component:
>
> $$\mathbf{A} = a_{iso}\mathbf{I} + \mathbf{T}, \qquad (3)$$
>
> where $\mathbf{I}$ is the identity matrix and $\mathbf{T}$ is the dipolar part of the hyperfine matrix. a_{iso} (typically in MHz), also known as Fermi's contact interaction, is proportional to the probability of finding the electron spin at the nucleus $\left(\left|\psi_{(0)}\right|^2\right)$:
>
> $$a_{iso} = \frac{2\mu_0}{3\hbar} g_e\beta_e g_n\beta_n\left|\psi_{(0)}\right|^2 = \frac{Tr(\mathbf{A})}{3}. \qquad (4)$$
>
> It follows from equation 4 that different isotopes of the same element will display isotropic hyperfine constants proportional to the corresponding g_n, for instance deuterium will have an isotropic hyperfine coupling ~ 6.5 times smaller than that of hydrogen.
>
> The dipolar part of the hyperfine matrix can be used to determine the distance r between an unpaired electron ($\mathbf{T}$ is proportional to $1/r^3$). In the EPR literature, A, a_{iso} and T are usually given, where
>
> $$A = [A_x, A_y, A_z] = a_{iso} + T. \qquad (5)$$
>
> $A_{x,y,z}$ are the principal components of the diagonalized hyperfine matrix and $T = [-T, -T, 2T]$ in axial symmetry.

obtained by other methods,[15] or reactive intermediates in microporous materials.[16] As shown in Figure 2B above, the hyperfine interaction results in further splitting of the energy levels and in simple cases A can be deduced directly from a field-swept EPR spectrum.

2.4   The Nuclear Quadrupole Interaction for nuclei with nuclear spin I > ½ (H_NQ)

The nuclear quadrupole coupling yields information on the bonding of I > ½ nuclei, e.g. the degree of sp hybridisation, such as distinguishing between an amine and an amide.

This interaction exists only for nuclear spins with $I > 1/2$ (e.g ^{2}H, ^{14}N), which possess a nuclear quadrupole moment. The nuclear quadrupole interaction stems from the interaction of the nuclear quadrupole moment (Q) with the electrical field gradient generated by the asymmetric distribution of the electron density (Box 5). The nuclear quadrupole interaction can be observed

when molecular tumbling is suppressed (since the trace of **Q** is zero, Box 5) but due to broadening its effects are often small and difficult to detect in field-swept EPR spectra. Nonetheless EPR spectra with narrow lines can display discernible peak shifts (no additional peak splittings are observed) resulting from the nuclear quadrupole interaction; for an example the reader is referred to Figure 8 and discussion in ref.[17].

The nuclear quadrupole interaction can be apparent in pulse EPR spectra, from which

---

Box 5: The nuclear quadrupole

The nuclear quadrupole term in the Hamiltonian is given by:

$H_{NQ} = \mathbf{IQI}$,

where the nuclear quadrupole tensor **Q** is traceless (it cannot be observed if the molecule tumbles rapidly). In the eigenframe it is given by

$$\mathbf{Q} = \frac{e^2qQ}{4I(2I-1)\hbar}\begin{pmatrix} -(1-\eta) & \square & \square \\ \square & -(1+\eta) & \square \\ \square & \square & 2 \end{pmatrix}. \quad (6)$$

The two quantities given in the literature are usually $(e^2qQ)/h$, the quadrupolar coupling constant, and η, the asymmetry parameter ($0<\eta<1$, where 0 designates axial and 1 rhombic symmetry).

Given that a comparison between quadrupolar coupling constants is meaningful only between nuclei with same I, in some cases the quantity $K = \frac{e^2qQ}{4I(2I-1)\hbar}$ is given in the literature.

---

the nuclear quadrupole coupling constant or K (see Box 5) can often be determined. Indeed K for ^{14}N nuclei can be a sensitive probe for the detection of hydrogen bonding.[15,18]

2.5   *The Nuclear-Nuclear Spin Interaction* (H$_{NN}$)

Although essential in NMR, nuclear-nuclear spin interactions are negligible in EPR given their small relative magnitude compared to electron-nuclear and electron-electron interactions.

2.6   *Strongly-coupled electrons: the zero-field splitting interaction* (H$_{ZFS}$)

The zero-field interaction can become very important when multiple strongly-coupled unpaired electrons are present (e.g. electrons located on the same transition metal ion).

When more than one electron spin is present the electron-electron coupling also has to be considered. Strongly-coupled unpaired electrons are well-described by a 'group spin', $S > 1/2$. The dipolar interaction and spin-orbit coupling between such strongly interacting electrons removes the ($2S+1$) degeneracy expected in the ground state – this zero-field splitting is, as the name suggests, present even in the absence of a magnetic field (Box 6). The two zero-field splitting parameters, D and E, depend on the average distance between the unpaired electrons

11

and the deviation from the cubic symmetry, respectively. When the energy of the microwave quantum exceeds the energy gap caused by the ZFS interaction (i.e. $h\nu \gg D$), both intra- and inter-manifold transitions are observed (see Box 6 and ref.[19]). If on the other hand $D \gg h\nu$, no inter-manifold and only the intra-manifold transition is observed. The intra-manifold transition can be treated as an *effective S = 1/2* spin system but with g values that may deviate substantially from those of a "true" $S = 1/2$ system. In this limit, interpretation tools called rhombograms[2] have been developed to correlate the effective g values to the ZFS parameters (E/D ratio). If the assumption $D \gg h\nu$ does not hold true, the measured g values do not follow the rhombogram predictions and may vary when measured at different magnetic fields.

Box 6: The zero-field interaction

The zero-field interaction tensor $\mathbf{D}$ is symmetric and traceless:

$$\mathbf{D} = \begin{pmatrix} D_x & \square & \square \\ \square & D_y & \square \\ \square & \square & D_z \end{pmatrix} = \begin{pmatrix} \frac{-D}{3} + E & \square & \square \\ \square & \frac{-D}{3} - E & \square \\ \square & \square & \frac{2D}{3} \end{pmatrix}, \qquad (7)$$

therefore only two parameters ($D = 3D_z/2$ and $E = (D_x - D_y)/2$) are needed to describe $\mathbf{D}$ in its diagonal form. For cubic symmetry $D = E = 0$ and the spin sublevels are degenerate; for axial symmetry $D \neq 0$ and $E = 0$, and for rhombic symmetry $D \neq 0$ and $E \neq 0$.

For the $S = 5/2$ example below with axial symmetry ($D > E = 0$, e.g. high-spin Fe^{3+}), the m_S sublevels $\pm 1/2$, $\pm 3/2$ and $\pm 5/2$ are non-degenerate and EPR transitions may be observable at zero field (brown double-headed arrows).
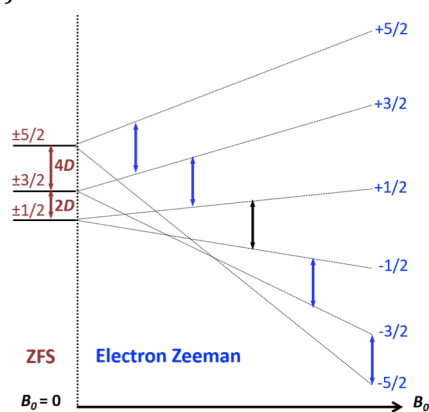
In the presence of B_0, the sublevels are split by the EZ interaction and the black vertical double-headed arrow indicates the *intra*-manifold EPR transition ($m_s = -1/2 \rightarrow m_s = +1/2$, which for a semi-integer spin is always detectable at any microwave frequency) whereas the blue ones indicate *inter*-manifold transitions.

2.7 *Weakly coupled electrons: the dipolar and exchange interactions* ($H_{DD} + H_{EX}$)

The dipolar interaction provides information on the distance and orientation between two weakly-coupled unpaired electrons. The exchange interaction can provide information on the type of coupling, e.g. antiferromagnetic or ferromagnetic.

When two (or more) weakly-coupled electrons are present (e.g. a bis-radical or a di-nuclear Cu^{2+} complex with a distance between the spins of ca. 15 Å or more), these are best described by

their individual spins, but with consideration of the interactions between them. The electron dipole-dipole interaction is a through-space interaction that, like the electron-nuclear anisotropic hyperfine interaction, depends on the distance r between two spins ($1/r^3$) and their relative orientation (Box 7). If there is overlap between the wavefunctions of the two electron spins, an additional contribution, stemming from the electron exchange interaction (Box 7), must be considered. In the simple case of two $S = 1/2$

Box 7: A closer look at weakly coupled spins

For *two weakly-coupled* electron spins (1 and 2) the spin Hamiltonian is given by:

$$H_0 = H_0(S_1) + H_0(S_2) + \textcolor{red}{H_{DD}} + \textcolor{red}{H_{EX}} \qquad (8a)$$
$$= H_0(S_1) + H_0(S_2) + \mathbf{S_1 D S_2} + \mathbf{S_1 J S_2}. \qquad (8b)$$

where $H_0(S_1)$ and $H_0(S_2)$ are defined by the energy terms given in Box 1. The electron dipole-dipole coupling tensor **D** (note that, confusingly, **D** is also used for the zero-field splitting tensor) is analogous to **T** (see Box 4):

$$\mathbf{D} = \frac{\mu_0}{4\pi\hbar} \frac{g_1 g_2 \beta_e^2}{r_{12}^3} \begin{pmatrix} -1 & \square & \square \\ \square & -1 & \square \\ \square & \square & 2 \end{pmatrix} = \begin{pmatrix} -\omega_{dd} & \square & \square \\ \square & -\omega_{dd} & \square \\ \square & \square & 2\omega_{dd} \end{pmatrix}. (9)$$

This point-dipole approximation of **D** is not always valid, especially when the *g*-anisotropy is large (e.g. transition metal ions) and the electron spin is highly delocalised (e.g. iron-sulfur clusters).

The electron exchange coupling tensor $\mathbf{J} = \begin{pmatrix} -J & \square & \square \\ \square & -J & \square \\ \square & \square & 2J \end{pmatrix}$ consists of an isotropic (J_{iso}) and an isotropic part. J_{iso} is usually sufficient to describe the exchange coupling:

$$H_{EX} = J_{iso}\mathbf{S_1 S_2}. \qquad (10)$$

Several conventions are used in the literature, ($-J_{iso}\mathbf{S_1 S_2}, 2J_{iso}\mathbf{S_1 S_2}, -2J_{iso}\mathbf{S_1 S_2}, J_{iso}(2\mathbf{S_1 S_2} - 1/2)$), so that it is important to check which expression was used in order to determine J_{iso}.

---

spins, the sign of the isotropic exchange interaction J_{iso} determines whether the singlet state (*antiferromagnetic* coupling, positive J_{iso}) or the triplet state (*ferromagnetic* coupling, negative J_{iso}) lies lower in energy. Because the electron exchange interaction decays exponentially with distance as the wavefunctions of the overlapping orbitals decay, J_{iso} normally tends to zero at distances greater than approximately 15 Å.

2.8 Relaxation (T_1 and T_2)

Fast relaxation times mean that many samples have to be measured in the frozen state. Provided that relaxation times are sufficiently fast, the sensitivity of an EPR experiment generally increases with decreasing temperature, as expected from the Boltzmann distribution.

In addition to the "static" interactions discussed in the previous sections, two dynamic relaxation processes play an important role in an EPR experiment: (1) The spin-lattice or longitudinal relaxation time T_1 characterises spins 'dropping' from the upper energy level to the lower level with excess energy dissipated through thermal vibrations of the lattice; (2) the spin-spin or transverse relaxation time T_2 characterizes the redistribution of energy within an ensemble of spins and occurs with no net energy change. In the absence of relaxation, the application of microwave radiation would equalise the populations of the lower and upper energy levels so that no net microwave radiation would be absorbed and no EPR signal observed. Relaxation, which re-establishes equilibrium populations, is thus required to remove this microwave "saturation" effect and allow observation of an EPR signal. On the other hand very fast relaxation, as often observed at room temperature for e.g. transition metal complexes, can lead to such extensive broadening of the spectrum (see equation 11 in Box 8) that effectively no EPR signal is observed.[1] Because T_1 and T_2 increase with decreasing temperature, such

> **Box 8: A closer look at relaxation**
> T_1 and T_2 are related to the (homogeneous) linewidth through the following equation:
> $$\text{half width} = \frac{1}{T_m} = \frac{1}{T_2} + \frac{1}{2T_1} \qquad (11)$$
> T_1 affects linewidths because it is related to the lifetime of the upper energy level: a long T_1 leads to sharper lines, and vice versa, as dictated by Heisenberg's uncertainty principle. T_2 affects the linewidth through spin-spin dipolar and exchange interactions.
> Given that T_1 (typically ms) >> T_2 (typically μs), T_2 tends to dominate the line broadening. T_m (the phase memory time) is a useful parameter to characterise the resultant linewidth, as well as the echo decay in many pulse EPR experiments.

'fast-relaxing' systems can often be investigated at cryogenic temperatures. Analysis of relaxation times and their dependence on molecular orientation in the applied magnetic field[20] can provide valuable insight into molecular and lattice dynamics, e.g. organic radicals and transition metals.[21]

2.9 Experimental considerations

Continuous wave (CW) measurements are usually the entry point for any EPR investigation. Pulse EPR measurements are needed to investigate a specific (e.g. hyperfine) interaction in detail and almost always require cryogenic temperatures (i.e. solid-state samples).

A basic knowledge of how EPR spectrometers operate[22] is required in order to acquire reliable data. Commercially available EPR spectrometers span a microwave frequency of 1 to 263 GHz (corresponding to a magnetic field of 0.03 to 9 T), but most EPR studies are conducted at 9 GHz (~0.3 T), the so-called 'X-band' frequency. Q-band frequency (~ 35 GHz) experiments are also relatively common. The naming of the different frequency bands in EPR has a historical origin dating back to the development of radars. EPR experiments conducted at higher microwave radiation (and hence magnetic field strength) can be more sensitive but are also usually more involved experimentally. Since fluid-solution EPR spectra are very sensitive to molecular motion and their shape reflects the complete or incomplete averaging of any magnetic interaction (e.g. g values, hyperfine interactions, dipolar interactions), it follows that the operating frequency (i.e. the applied microwave frequency, ν_{mw}) can greatly affect the appearance of the spectrum. For example, a radical with anisotropic axial g values of $g_{x,y}$ = 2.15 and g_z = 2.00 will give rise to an EPR spectrum with a single line at g_{iso} = 2.10 provided that the radical tumbling time is *less* than the $1/\nu_{mw}$ (e.g. 100 ps at 9.5 GHz or 10 ps at 95 GHz). Conversely, if the radical tumbling time is *greater* than $1/\nu_{mw}$, the EPR spectrum will show two lines, a superposition of g_z and $g_{x,y}$. The above generalisation only holds true when the magnetic anisotropy is relatively small; a larger anisotropy requires lower operating frequency or faster tumbling to be averaged out. Indeed, an intermediate regime between these two extremes is most commonly observed. In summary, dynamics that are fast at X-band, and lead to a complete averaging of the magnetic anisotropies, may appear slow at W-band. Sample conditions such as solvent viscosity and temperature can also have a profound effect on EPR spectra given their influence on molecular dynamics.

2.9.1   CW EPR

In a CW experiment the sample is irradiated continuously by low-intensity monochromatic microwave radiation. As the magnetic field is swept over a defined range, different EPR transitions are brought into resonance by the applied microwave radiation. CW field-swept spectra are typically measured and presented as derivatives because a modulation-amplitude detection method is used experimentally. This method of detection leads to an increased signal-to-noise ratio. Although convenient and often the first step required for a more in-depth study, CW EPR usually suffers from limited spectral and time resolution. Similar to NMR, CW EPR spectra simplify considerably when recorded in fluid solution, i.e. when molecules are free to tumble and magnetic interactions are averaged such that only isotropic components survive: in fluid solution all molecules are equivalent and experience the same average interaction with the applied magnetic field (see Figure 2A and ref. [1] for a detailed description). In frozen solution the orientation of each molecule is fixed with respect to the applied field and consequently the magnitude of the interactions is different. The CW spectrum of a frozen solution is a weighted sum of all the possible molecular orientations. Therefore, all but the largest electron-nuclear spin interactions (hyperfine couplings) are masked by the relatively broad linewidths.

Box 9: Anisotropy in pulse EPR

The large anisotropy of some powder/frozen samples (i.e. their EPR spectra span a large magnetic field range) can be used to derive orientation-specific information, for example the measurement of A_z specifically. That is, measurements at specific field positions can yield "single crystal-like" information, i.e. as if measuring a single crystal in a specific orientation with respect to the applied magnetic field.

However, in many cases the full set of magnetic parameters (e.g. A_x, A_y, A_z) cannot be determined 'by eye' from a single spectrum. Simulation of spectra acquired at a set of different field positions is required because of 'orientation selection', i.e. the applied microwave pulse cannot excite the entire EPR spectrum (for example, an Fe-S cluster spectrum typically spans 40 mT when the microwave pulse excitation bandwidth is only a few mT). However, the recent introduction of shaped and composite pulses, which open the possibility of independently tuning the amplitude and phase of microwave pulses, already improves excitation bandwidths, can remove orientation selection, and promises to revolutionise EPR spectroscopy.[14]

2.9.2   Pulse EPR

Akin to modern NMR, in a pulsed EPR experiment the field is kept constant and the sample is irradiated with short (nanosecond) and high-intensity microwave pulses. A pulsed experiment enables isolation, detection and measurement of the interactions that contribute to

the shape and behaviour of a CW spectrum (Box 9). Importantly, pulse EPR experiments can be designed to address a specific interaction (i.e. a specific term in the spin Hamiltonian, Box 1). Because relaxation times are too short at room temperature, pulsed EPR measurements normally require cryogenic temperatures. In the examples discussed in Sections 4 and 5 we thus restrict our discussion to powder and frozen-solution samples. The requirement for solid-state samples for pulse EPR has the advantage that we can measure dipolar magnetic interactions that are suppressed by motional averaging in liquid solution.

2.9.3 Pulse EPR experiments

Here, we briefly introduce some of the most common pulse EPR experiments that are referred to in the following sections. For full descriptions, including pulses sequences, see ref. [12].

Echo-detected field sweeps (Box 10): These may be regarded as analogous to CW field-swept spectra, except that spectra are recorded and shown as absorption spectra rather than derivatives.

ENDOR: In electron-nuclear double resonance (ENDOR) experiments, NMR transitions (i.e. transitions involving nuclear spin flips, which are nominally EPR-forbidden) are driven by a radiofrequency radiation. ENDOR often provides very useful information on strongly coupled nuclei, e.g. those in the first coordination sphere of the electron spin. For a

<div style="border:1px solid black; padding:10px;">

Box 10: Echo-detected EPR

NMR experiments are mostly based on the detection of the Free Induction Decay (FID) of magnetization after a radiowave pulse (A):
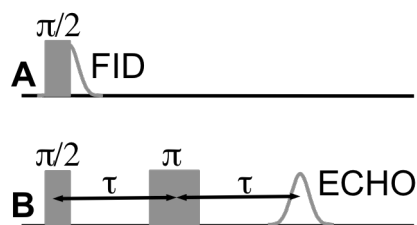
In EPR, the FID is often too short-lived and spectra are often too broad to be excited by a single microwave pulse. Thus a spin echo detection is preferred (B). By recording the intensity of the spin echo at different magnetic fields the EPR spectrum can be reconstructed (giving an echo-detected field sweep). Relaxation times (T_2) and the ESEEM effect can be measured by varying the interpulse delay τ at a fixed magnetic field.

</div>

tutorial review on ENDOR spectroscopy, including continuous-wave ENDOR and the most common Mims and Davies pulse sequences, the reader is referred to ref. [6].

ESEEM: The information derived from electron spin echo envelope modulation (ESEEM) experiments is analogous to that obtained from ENDOR, i.e both experiments may be regarded as an NMR spectrum of the paramagnetic compound, with the exception that ESEEM typically detects more weakly coupled nuclei (e.g. those in the second coordination sphere of the electron spin). ESEEM consist of a series of microwave pulses at a single microwave frequency separated by fixed and variable time intervals. The resulting electron spin echo is then recorded as a function of the variable time interval. The pulse sequence induces modulation of the amplitude of the detected electron spin echo that results from magnetic nuclei in the spin system, and yields a modulated time domain signal (similar to a Free Induction decay). Fourier transformation then allows identification of nuclear frequencies and corresponding hyperfine couplings. For a discussion of different ESEEM experiments (2-pulse and 3-pulse ESEEM), including their advantages and disadvantages, the reader is referred to ref. [23].

HYSCORE: When more than one hyperfine coupling is expected to be present, the two-dimensional counterpart of ESEEM – HYSCORE (Hyperfine sublevel correlation) spectroscopy – is often the method of choice. HYSCORE spectroscopy correlates nuclear transition frequencies (ν_α, ν_β) in the α and β electron-spin manifolds (see Figure 2Bi). The spectrum is divided into two quadrants: signals in the right-hand-side (+,+) quadrant typically originate from weakly coupled nuclei ($|A| < 2|\nu_I|$, where ν_I is the Larmor frequency of the nucleus), whereas those in the left-hand-side (–,+) quadrant usually result from strongly coupled nuclei ($|A| > 2|\nu_I|$). The nature of the coupled nucleus can be identified by the position of the peaks in the spectrum, e.g. weakly-coupled ^1H are centred around the Larmor frequency of the proton (ca. 15 MHz at X-band). The spatial separation of different types of nuclei, and whether they are weakly-coupled or strongly-coupled explains the popularity of HYSCORE. This technique is however much more time-consuming than one-dimensional ESEEM.

DEER: The double electron-electron resonance (DEER) experiment is often the method of choice to measure the distance between two weakly-coupled electron spins. It is a two-frequency (pump and probe) experiment that measures the electron dipole-dipole interaction between

two spins, which varies inversely with their cubed distance. The first microwave frequency is used to select a fraction of the spins (probe) and to produce the measured signal (echo). A second microwave frequency (pump) is used to invert the orientation of the coupled spin, causing a modulation of the signal (echo) intensity at the frequency of the electron spin-spin coupling (known as the dipolar frequency).

2.10 Spectral interpretation

Simulation is usually required for the interpretation of EPR spectra but is increasingly accessible to non-specialists.

Few spectra can be fully and easily interpreted by measuring peak positions and separations like in one-dimensional NMR (Box 11). Spectral interpretation is often the most time-consuming aspect of any EPR study and usually requires simulation of the EPR spectra. Historically, simulations were a major bottleneck, with each research group having to develop

> **Box 11. Why is the interpretation of EPR spectra not straightforward?**
>
> EPR spectra often depend on the magnitude and relative orientation of all magnetic tensors (**g**, **A**, **Q**, **D**) with respect to each other and with respect to the applied magnetic field. This leads to many parameters, but simulations often allow the determination of these tensors and their relative orientation.
>
> In some cases (e.g. when many interactions are of similar magnitude), fitting of the experimental data based on a full quantum mechanical computation (density functional theory) and molecular dynamics simulations is necessary for reliable spectral interpretation.

their own programmes. Nowadays a number of excellent packages are available. One of the best is *EasySpin*, a toolbox supported by MATLAB for simulating and fitting CW and pulsed EPR spectra (http://easyspin.org).[24,25] The now widespread use of *Easyspin*, which is freely available, enables consistent analysis and allows non-experts to simulate most EPR spectra. EPR spectrometers manufacturers have also developed simulation packages (e.g. *XSophe* by Bruker). In addition, the fast open-source spin dynamics programme *Spinach* covers magnetic resonance applications, including EPR (http://spindynamics.org/Spinach.php).[26] Finally, the on-line educational tool *EPR simulator* (http://www.eprsimulator.org),[2] enables the user to see the

---

[2] EPR Simulator is under construction and being developed by Dr. Victor Chechik, University of York (UK).

effect of different EPR parameters on simulated spectra (e.g. Cu(II), nitroxides, radicals in solution) in an interactive manner.

3   What g values can tell us and the benefit of multiple frequencies (H$_{EZ}$)

In this section we discuss how the interaction between a paramagnet and the applied magnetic field leads to the appearance of an EPR line at a characteristic g value that depends on the molecular environment and the electronic ground state. Owing to their dependence on spin-orbit coupling, g values are much more difficult to predict than NMR chemical shift values and tables correlating g with structural motifs are limited.[27,28] Nonetheless, g values can be important parameters in EPR characterisation. The relevance of g as an observable to characterise the electronic state and molecular geometry, and the detection of mechanistically-relevant bonding interactions is illustrated below. The advantages of multi-frequency EPR to disentangle composite spectra will also be apparent.

3.1   Detecting the presence of different species and deducing electronic configurations

Motivated by the role that Ti(III) compounds play in homogeneous and heterogeneous catalysis (e.g. Ziegler-Natta polymerisation), Chiesa, Van Doorslaer and co-workers investigated $TiCl_3(Py)_3$ and $TiCl_3$ complexes.[29] Continuous-wave EPR spectra at multiple microwave frequencies (Figure 3) revealed the presence of two distinct rhombic Ti(III) ([Ar]3d^1, hence $S =$ 1/2) species. The g values of the peak positions remain unchanged with increasing magnetic field, indicating that any magnetic interaction between the centres is negligible (see, in contrast, Section 3.2). The two Ti^{3+} species could in fact be ascribed to defects in the solid, ligated by ^{14}N nuclei (as revealed by pulse EPR experiments, not discussed here). In this case, the only magnetic interaction that needs to be considered is the EZ interaction for the two Ti(III) species since other interactions are not resolved (i.e. the spin Hamiltonian is well described by H$_{EZ}$, see equation 1, Box 1). Note that the peaks appear sharper, on a g-value scale, at higher microwave frequencies because they are further apart on a magnetic field scale, while the linewidths do not increase proportionally with the field. This is analogous to NMR experiments carried out at

different operating frequencies, where however the effect is less apparent since NMR peaks are generally much sharper (Section 1.1).
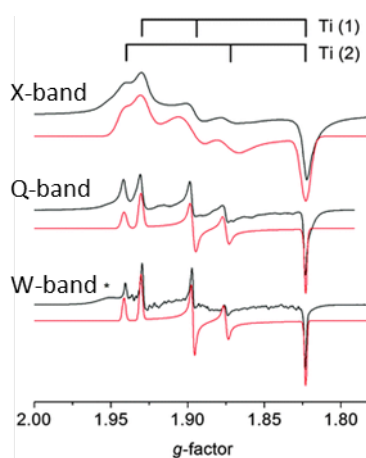

Figure 3. Two distinct Ti(III) species present in powder TiCl$_3$(Py)$_3$, as revealed by multifrequency EPR. Simulated EPR spectra are in red. Adapted from ref.[29] with permission from the PCCP Owner Societies.

All six principal g values of the two Ti(III) species are below g_e. This illustrates that generally $g<2$ for transition metal complexes with configuration $d^{n,n<5}$, conversely $g>2$ for $d^{n,n>5}$ and $g\sim g_e$ for d^5 complexes (e.g. high-spin Mn^{2+}). The relatively large g anisotropy (Section 2.1) is a reflection of the effective spin-orbit coupling constant that increases with increasing nuclear charge (excited states are closer to the ground state).

g values can also yield information on the electronic ground state and the geometry of metal complexes. A classic example is Jahn-Teller distorted Cu^{2+}. The vast majority of Cu^{2+} complexes exhibit a 'lengthening' of the z axis (tetragonal distortion), resulting in the unpaired electron being in the x^2-y^2 3d orbital ($g_z > g_{x,y}$). Halcrow and co-workers[30,31] have shown that simple substitution by more bulky substituents in the ligand framework can result in 'shortening' of the z axis (a much less common type of tetragonal distortion), and thus in the unpaired electron being in the z^2 3d orbital, i.e. $g_z < g_{x,y}$ (see Figure 4, left). This is clearly apparent in the Q-band (~35 GHz) CW EPR spectra (Figure 4, right). Note that the hyperfine coupling of the electron spin to the Cu nuclear spin ($I = 3/2$, $2I + 1 = 4$) is, as is often the case, only resolved along g_z.
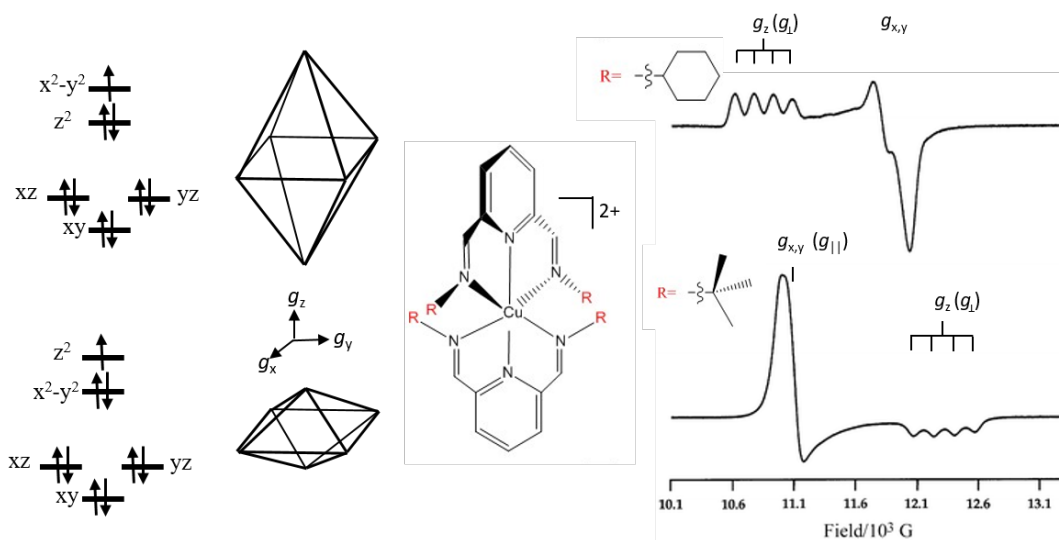
Figure 4. Illustration of the g value serving as an observable to characterise the electronic ground state and molecular geometry. Note that in the axial case, $g_{\parallel}$ is typically used to designate $g_x = g_y$ and $g_{\perp} = g_z$. Figure adapted from ref. [31] with permission from The Royal Society of Chemistry.

3.2 Inferring magnetic coupling between centres through g values

EPR spectroscopy led to the discovery of iron-sulfur (Fe-S) clusters, which are now recognised to be ubiquitous in nature and assume a wide range of roles ranging from electron transfer to participation in catalysis. It was long a puzzle how two Fe ions (high-spin Fe^{3+}, $S = 5/2$, and Fe^{2+}, $S = 2$, both have expected g values above g_e) give rise to an average g value *below* g_e. Long before the first crystallographic structures became available, Gibson *et al.*[32] predicted an antiferromagnetic exchange interaction between the Fe centres, forming a [2Fe-2S] cluster, that explains the experimentally observed g values and the total spin $S_{total} = S_{Fe(III)} - S_{Fe(II)} = \frac{1}{2}$ ground state (Figure 5).
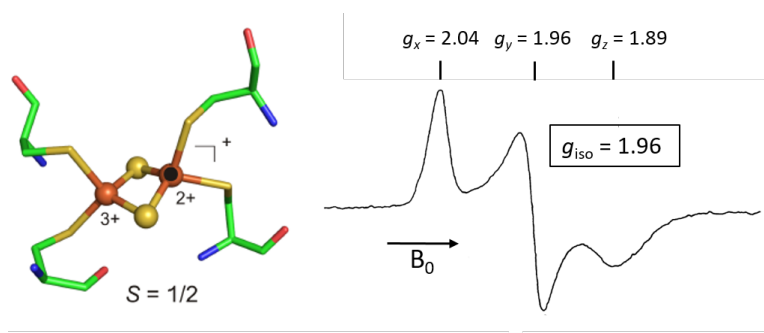

Figure 5. The structure of a typical [2Fe-2S] cluster, as found in e.g. spinach ferredoxin (left) and corresponding X-band EPR spectrum[33] (right), illustrating that antiferromagnetic coupling between the

Fe centres results in a single unpaired electron with an average (isotropic) g value below g_e. Colour coding: Fe = orange, S = yellow, N = blue, O = red, protein backbone = green.

3.3   Detecting mechanistically relevant bonding interactions

Radicals are involved in numerous redox reactions and biological electron transfer, and deciphering their bonding interactions is of mechanistic relevance. Stoll *et al.* showed that hydrogen bonding to tryptophan radical cations is reflected in a change in the g anisotropy.[34] The very small shift of g_x by just 0.00015 (Figure 6), that could be predicted by density functional theory, is only detectable at extremely high magnetic fields/frequencies (700 GHz). Pulse ENDOR (Section 2.9) at lower frequencies (X- and Q-band) however could detect the H-bonded proton by comparison with the deuterated sample. The very different magnetic properties of ^{1}H ($I = \frac{1}{2}$) and ^{2}H ($I = 1$) mean that deuteration is commonly employed to detect and characterise exchangeable protons, and the effects of isotopic substitution on EPR spectra are discussed further in Section 4.4.
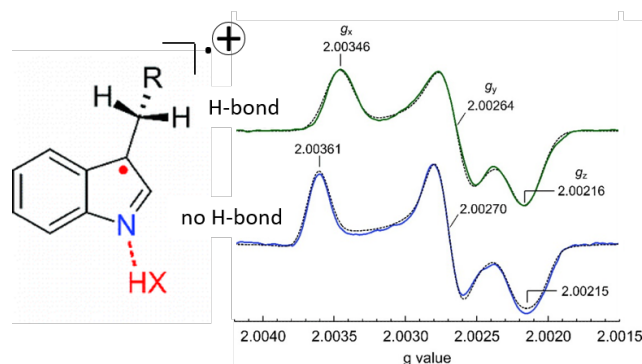

Figure 6. Illustration of how g values can be sensitive to relatively weak bonding interactions. The g_x of the tryptophan radical cation shifts with hydrogen bonding, as revealed by very high-frequency EPR (700 GHz). In deuterated samples the proton of HX (in red) is replaced by D. Adapted with permission from [34]. Copyright 2011 American Chemical Society.

All discussion in this section was restricted to $S = 1/2$ systems. Large deviations from g_e can occur in systems with multiple unpaired electrons (see Section 5).

4 Nuclei surrounding the unpaired electron spin: Hyperfine and nuclear quadrupole interactions (H$_{HF}$ & H$_{NQ}$)

In this section we will show that a wealth of information can be extracted from the interaction between unpaired electrons and surrounding nuclei, that not only encodes structural but also functional and mechanistic information. In the examples below, the reader will be introduced to some of the most common experiments used to measure and gain more detailed information from hyperfine interactions. More than a single EPR method is often suitable (and necessary) to solve a particular problem, and the examples below have been chosen to illustrate different hyperfine EPR experiments (see Section 2.9.3).

4.1 Fe(I) intermediate in catalysis (CW EPR)

Organometallic Fe(I) compounds are rare but were recently shown to be important intermediates in Negishi cross-coupling reactions through EPR experiments.[35] Continuous-wave EPR spectroscopy of a likely Fe(I) intermediate shows that the unpaired electron is primarily located on the low-spin Fe centre (S = 1/2), with a near-axial g tensor (Figure 7) whose anisotropy was reproduced in DFT calculations. Moreover, large hyperfine couplings to four nearby phosphorus atoms (I = 1/2) are clearly visible. From the 1:4:6:4:1 quintuplet pattern apparent in the g_1 region[3] and on the basis of the structure one may be led to conclude that the strength of the hyperfine coupling to the Fe(I) electron spin of the two (equal) equatorial P is very similar to the two (equal) axial P. However, as revealed through simulation of the *entire* EPR spectrum, the equatorial ^{31}P are actually *inequivalent* and one is more weakly coupled (a_{iso} = 37.9 MHz, T = [2.9, –5.7, 2.7] MHz, see Box 4) relative to the remaining P ligands with similar coupling parameters (a_{iso} = 71 MHz, T = [2.8, –1.4, –1.4] MHz). EPR experiments thus demonstrated unambiguously that Fe(I) is present in such cross-coupling reactions, and that the complex adopts a distorted geometry in solution as shown by the inequivalent spin density distribution onto the ^{31}P ligands.

---

[3] Note the notation $g_{1,2,3}$ (rather than $g_{x,y,z}$) is used in this case because the g values were not assigned to the Cartesian axes.
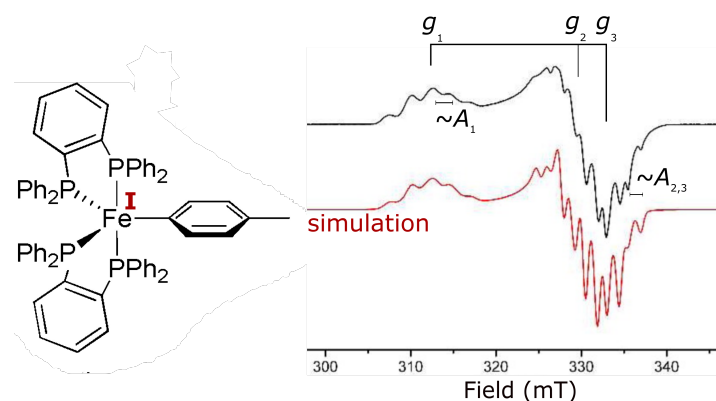
Figure 7. Fe(I) complex in Negishi cross-coupling reactions (left, schematic structure) and corresponding X-band CW EPR spectrum and simulation (right) demonstrating that the unpaired electron is mostly located on Fe. Note that the indicated hyperfine couplings A are very approximate but serve as a good starting point for simulations (a useful rule of thumb is that 1 mT $\sim$ 28 MHz for g $\sim$2). Adapted with permission from [35]. Copyright 2012 American Chemical Society.

4.2 Host-guest interactions (ENDOR)

Unless the hyperfine coupling to the electron spin is relatively large (tens of MHz), it is often not observed in CW EPR in the solid state. We now discuss an example of a much subtler interaction. Turro and co-workers investigated the magnetic communication between a fulleride radical anion host cage and a H_2 guest molecule encapsulated within it (Figure 8). The H_2 guest can be in the ortho (I = 1) or para (I = 0) nuclear spin state.[36] The CW EPR spectrum (Figure 8A) is dominated by three lines of approximately equal intensity, arising from the unpaired electron delocalised over the surface of the fulleride coupling to the nearby ^{14}N atom with I = 1 (additional low-intensity lines arise from coupling to ^{13}C atoms of low natural abundance). However, pulsed ENDOR spectroscopy revealed the weak coupling between the unpaired electron and the endo-H_2 molecule through difference spectra (Figure 8B). In this "weak-coupling case" ($\nu_I > A/2$), the observed peaks are centred around the Larmor frequency of the proton ($\nu_I \approx 14.8$ MHz) at the measurement field as shown in Figure 8B (A = [0.35, 0.35, $-$1.00], i.e. a_{iso} = $-$0.10 MHz and T = $-$0.45 MHz, see Box 4). On the basis of the magnetic interaction between the fulleride and the H_2 molecule, demonstrating that cage and host molecule 'communicate', and the observed temperature dependence of the ENDOR spectra (not discussed here) showing that the *ortho-para* interconversion takes no longer than 1 hour, the

25

authors conclude that spin catalysis is highly efficient and may lead to a new way of driving *ortho*-H_2/*para*-H_2 conversion.
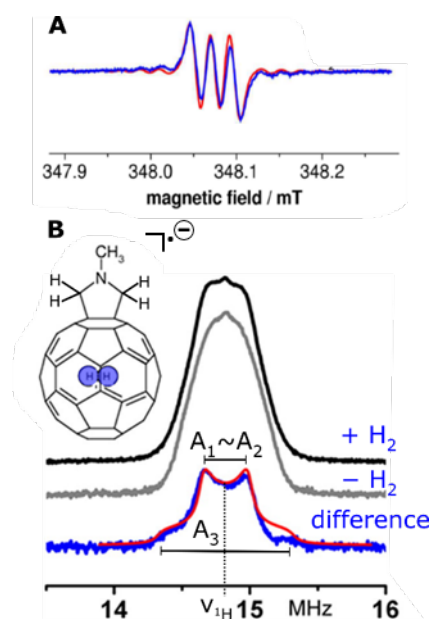

Figure 8. (A) CW EPR spectrum of the fulleride radical anion pictured in B with endo-H_2 (simulated spectrum in red). (B) Davies ENDOR EPR spectra of the fulleride in the presence (black) and absence (red) of the endo-H_2 molecule, and the difference spectrum (blue), with simulation (red). Adapted with permission from [36]. Copyright 2012 American Chemical Society.

4.3   The interstitial atom in the nitrogenase MoFe cluster (ESEEM)

The co-called MoFe cluster is one of the most complex clusters found in nature and being paramount for 'fixing' N_2 (breaking the nitrogen triple bond to form ammonia), by a mechanism that is not fully understood, continues to be an inspiration for biochemists and chemists alike. The nature of the central interstitial atom (formally coordinated by six bonds) was long a debate that EPR spectroscopy has helped to resolve in conjunction with high-resolution X-ray crystallography.[37] Upon labelling with ^{13}C ($I = \frac{1}{2}$), ESEEM revealed a small hyperfine coupling of 2.5 MHz (see inset in Figure 9) centred around the Larmor frequency peak of ^{13}C at 3.7 MHz, showing that the central atom is, surprisingly, carbon.
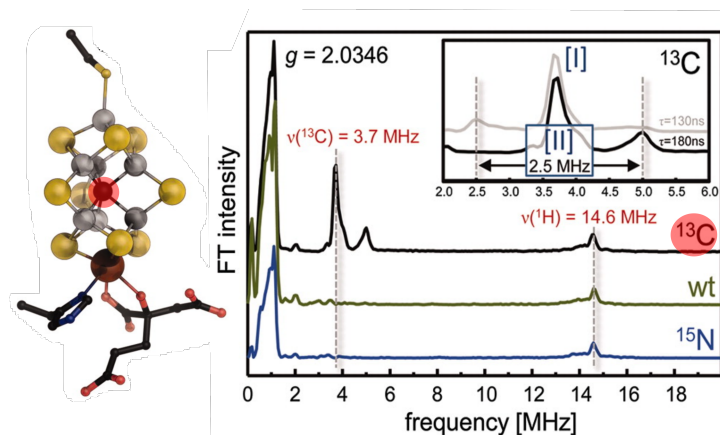
Figure 9. The MoFe cluster found in nitrogenases showing the usual central C atom with nominally six bonds (left; colour coding: Fe = grey, S = yellow, Mo = brown, central C = highlighted red, protein backbone = black, O = red, N = dark blue) and 3-pulse ESEEM spectra in the frequency domain of the wild-type (wt), ^{15}N- and ^{13}C-labelled protein. The inset show experiments acquired at different τ values (see Box 10); this is a requirement for 3-pulse ESEEM experiments because these are affected by blind spots (a suppression effect where individual peaks in the spectrum can disappear completely). Adapted from [37]. Reprinted with permission from AAAS.

4.4   Distinguishing between possible reaction intermediates (HYSCORE)

HYSCORE spectroscopy can be used to elucidate catalytic mechanisms and a powerful strategy is to combine HYSCORE with isotopic labelling. This can allow detection of usually silent nuclei (e.g. ^{12}C to ^{13}C, $I = 1/2$, substitution) or spectral simplification (e.g. ^{14}N, $I = 1$, to ^{15}N, $I = \frac{1}{2}$, substitution). As seen is Section 2.8.3, HYSCORE can distinguish between strongly and weakly coupled nuclei, providing means to characterise intermediates structurally and validate or rule out possible catalytic reaction pathways. Fugate et $al.$ [38] used HYSCORE to distinguish between three intermediates proposed to lead to the formation of biotin, an essential vitamin. The structure of the intermediate deduced from the spectroscopic data is composed of a reduced [2Fe-2S] cluster with a total spin $S = \frac{1}{2}$ ground state (see Section 3.2) bonded to 9-mercaptodethiobiotin (MDTB) as shown in Figure 10C. Selective ^{13}C labelling of MDTB revealed signals (correlation ridges), centred around the Larmor frequency of ^{13}C (3.8 MHz at 355 mT), that were not visible in the natural-abundance sample (Figure 10A); the relatively large a_{iso} (2.7 MHz, see Box 4) shows that significant electron density is on the ^{13}C atom, suggesting that it is directly bonded to the Fe-S cluster, as corroborated by the relatively large axial anisotropy ($T = 1.5$ MHz, Box 4). The simulated spectrum of the ^{13}C coupling (in the absence of orientation

27

selection, see Box 9) is shown in Figure 10Aii (right) – note that the experimental spectrum (Figure 10Aii, left) shows only part of the full ridge required to determine the hyperfine parameters (and hence a_{iso} and T) directly from the spectrum.
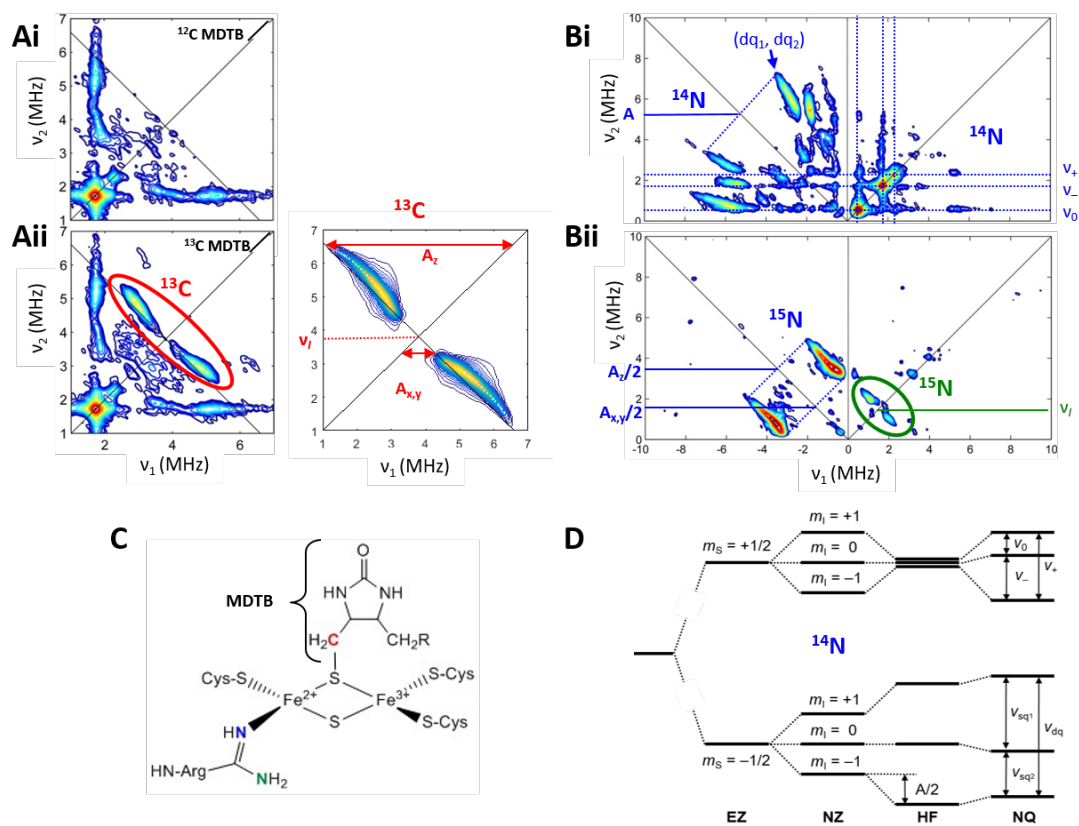

Figure 10. Spectroscopic evidence for the [2Fe-2S]–MDTB intermediate in the biosynthetic pathway of biotin. (Ai) and (Bi) HYSCORE spectra of the native protein bound to MDTB. (Aii) *left*: HYSCORE spectrum with ^{13}C-labelled MDTB and (Aii) *right*: simulated spectrum for the ^{13}C coupling in the absence of orientation selection. (Bii) HYSCORE spectrum with ^{15}N-labelled arginine; note that in this case, the hyperfine parameters from the strongly-coupled ^{15}N can be estimated quite accurately from the spectrum, despite orientation selection. (C) Spectroscopically deduced structure of the [2Fe-2S]-MDTB intermediate. (D) Energy-level diagram for a ^{14}N nucleus in the 'cancellation' condition. Adapted with permission from [38]. Copyright 2012 American Chemical Society.

Indicative of the two inequivalent N in the side-chain Arginine, the HYSCORE spectrum of the ^{15}N-Arg substituted enzyme (Figure 10Bii) shows the presence of two sets of peaks, centred around $-A/2$ in the left-hand quadrant (resulting from the strongly-coupled blue N in Figure 10C) and the Larmor frequency of ^{15}N in right-hand quadrant (resulting from the weakly-coupled green N in Figure 10C), respectively. The corresponding ^{14}N spectrum is considerably more complicated; up to 18 cross-peaks may be observed owing to the quadrupole moment

arising from the $I = 1$ nucleus. Usually the most prominent (often sole) peaks are those arising from the so-called double-quantum (dq) transitions ($\Delta m_I = \pm 2$ in each m_S manifold, Figure 10D) and the hyperfine coupling A can be estimated from these (Figure 10Bi). Determining the nuclear quadrupole parameters can be useful to deduce structural information such as the degree of sp hybridisation and hence coordination of the N nucleus in question.[39] Although this is often a challenging task, for the strongly-coupled ^{14}N in this example they are readily obtained because the NZ and HF interactions are of similar magnitude and approximately cancel each other out (i.e. combined they have no net effect on the energy levels) in one of the m_S manifolds (i.e. $2|\nu_I| \approx |a_{iso}|$, here the Larmor frequency of ^{14}N at field of the measurement, 347.5 mT, is 1.1 MHz and a_{iso} = 3.5 MHz), as illustrated in Figure 10D. The nuclear quadrupole transitions ν_0, ν_- and ν_+ ($\nu_0 = 2K\eta$, $\nu_+ = K(3 + \eta)$ and $\nu_- = K(3 + \eta)$, where $\nu_0 + \nu_- = \nu_+$ and $K = e^2qQ/4h$ (in MHz) for $I = 1$, see also box 5) are then directly observable (Figure 10Bi) and nuclear quadrupole parameters e^2qQ/h and η can be determined easily.[40] This "cancellation" or "matching" condition is surprisingly common for ^{14}N because it occurs even when $2|\nu_I|$ does not appear to match $|a_{iso}|$ very well. In fact, ν_0, ν_- and ν_+ are observed as long as $|\nu_I \pm |a_{iso}|/2|/K \sim 0.75 - 1$ (in the example given this ratio approaches the upper limit of 1). In many cases, the condition can be deliberately achieved by changing the microwave frequency.[41]

5   More than one unpaired electron (H_{ZFS}, H_{DD} and H_{EX})

For species with more than one unpaired electron ($S > 1/2$) the mutual interaction between the unpaired electrons must be considered. High-spin centres are common for transition metals and organic chromophores excited to their triplet (or higher order) state with laser irradiation, and these will be the focus of our discussion here. Pairs of weakly interacting spins (2 x $S = 1/2$) engineered onto diamagnetic molecules represent a special case of multiple unpaired electrons and are becoming increasingly popular in structural biology for distance determination.

5.1   Metal centres

Owing to their partially occupied *d* orbitals, transition metals often possess unpaired electrons and are thus amenable to EPR studies. In the EPR literature, low-spin refers to $S = 1/2$ systems whereas high-spin pertains any $S > 1/2$ system; the terminology thus differs from that of coordination chemistry (e.g. a "low-spin" d^4 octahedral complex is termed a high-spin $S = 1$ system in EPR). When there is a considerable exchange interaction between two or more spins (e.g. two metal centres sharing a μ-oxo bridge or two radicals covalently linked together) it is often convenient to define a total spin S_{total}. If spins are ferromagnetically coupled, S_{total} is the sum of the individual spins. For anti-ferromagnetically coupled spins, S_{total} is the difference of the individual spins (see Sections 3.2 and 5.1.2 for examples).

Integer spins ($S = 1, 2...$) are often difficult to observe in standard (parallel-mode) EPR because the zero-field splitting (ZFS, Section 2.6, Box 6) usually exceeds the energy of the microwave photons and their study typically requires high microwave frequencies beyond the conventional X- to W-bands. The ZFS varies greatly amongst different metal ions and coordination geometries as it depends on the spin-orbit coupling (see Section 3.1 for the effect of spin-orbit coupling on *g*), for instance it is very small for symmetric Mn(II) complexes and very large for octahedral Co(II) complexes. A comprehensive review on (high-field) EPR of mononuclear transition metal complexes can be found in ref. [42].

5.1.1   Interaction between multiple spins (exchange coupling)

With the goal to employ molecular nanomagnets as possible qubits (a qubit is a quantum bit of information) Winpenny, McInnes and co-workers used supramolecular chemistry to link two {Cr$_7$Ni} heterometallic rings ($S_{total} = 1/2$, due to antiferromagnetic coupling between 7 Cr(III) ions ($S = 3/2$), and 1 Ni(II) ($S = 1$), Figure 11B) to a Co (II) complex ($S = 3/2$). In this three-spin system, the central Co atom is exchange coupled to the neighbouring {Cr$_7$Ni} heterometallic rings (Figure 11A). EPR was used to determine the weak interactions between molecular components in the supramolecular structure that are undetectable using magnetometry. The ZFS of the central cobalt is too large to allow detection of inter-manifold EPR transitions (see

Box 6, even at 94 GHz). The Co^{2+} complex can be treated as an 'effective' $S = \frac{1}{2}$ system with 'characteristic' g-values that differ greatly from g_e: $g_z = 6.5$ (occurring at $\sim 1,000$ mT in Figure 11C), $g_y = 4.3$ ($\sim 1,600$ mT) and $g_x \approx 2$ ($\sim 3,500$ mT). The two heterometallic rings give rise to EPR signals at $g_{x,y} = 1.78$ and $g_z = 1.74$, that partially overlap with the g_x signal of the Co(II) centre (Figure 11C). The four additional splittings (a doublet of doublets) of g_z and g_y are a manifestation of the anisotropic exchange coupling (see Box 7) in the three-spin system and their values can be estimated from the spectrum.
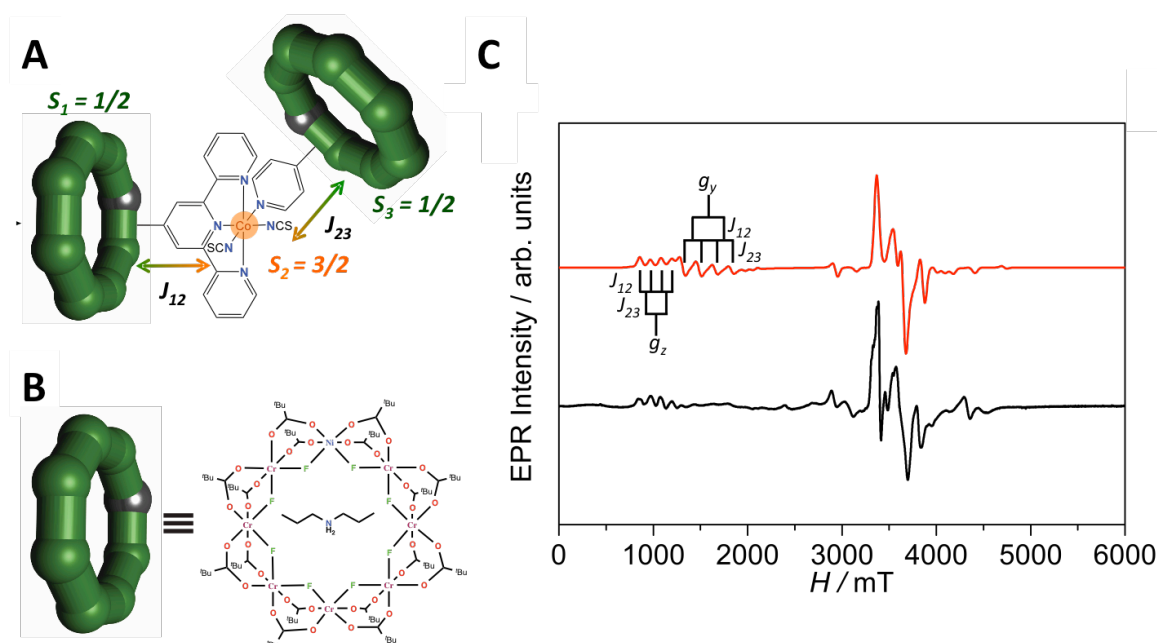

Figure 11. Determining interactions in a nanomagnet using EPR. (A) Schematic structure of the supramolecular three spin complex. The exchange coupling constants are indicated for each spin pair. (B) Structure of the polymetallic ring. In (A) and (B) Cr and Ni are represented as green and silver spheres, respectively. (C) Experimental W-band (94 GHz) spectra of the three spin system at 5K (black line) and corresponding simulation (red line). The exchange coupling pattern along g_z and g_y is indicated. Adapted from ref. [43].

5.1.2   Structural analysis of unusual Fe-S clusters (ZFS parameters, D & E)

Hydrogenases are enzymes that catalyse the interconversion of protons and hydrogen and are a benchmark for efficient H_2 production with earth-abundant metals. HydG, an enzyme required for the assembly of [FeFe]-hydrogenases, harbours two [4Fe-4S] clusters. One of these is instrumental for the synthesis of the [FeFe] active site and can reversibly coordinate a fifth Fe atom yielding an unprecedented [5Fe-5S] cluster. The addition of a Fe^{2+} ($S = 2$) centre to a [4Fe-4S]$^+$ cluster (with $S_{total} = \frac{1}{2}$ in this case) generates a new spin system with total spin either $S =$

5/2 (ferromagnetic coupling) or S = 3/2 (antiferromagnetic coupling). The [5Fe-5S] and [4Fe-4S] clusters are readily distinguishable in the CW EPR spectrum: The high-spin [5Fe-5S] cluster (a mixture of S = 3/2 and 5/2) appears at low magnetic field (Figure 12A) whereas the low-spin [4Fe-4S] cluster (S = 1/2) appears around g = 2 (Figure 12B).[44] With the aid of the corresponding rhombogram for a S = 5/2 spin system (Box 6), the four effective g values observed for the [5Fe-5S] cluster are readily assigned: g = 9.5 arises from the m_S = ± 1/2 manifold (i.e. one of the m_s = –1/2 → m_s = +1/2 transitions)[4] and g = 4.7, 4.1, 3.8 arise from the transitions within the m_s = ± 3/2 manifold (i.e. m_s = –3/2 → m_s = +3/2, in different orientations), from which the rhombicity can be determined as E/D = 0.225 (Figure 12D, see also Section 2.6). EPR spectroscopy thus provided evidence for the usual [5Fe-4S] cluster whose high-spin nature enabled its characterisation without interference from the low-spin [4Fe-4S] cluster.
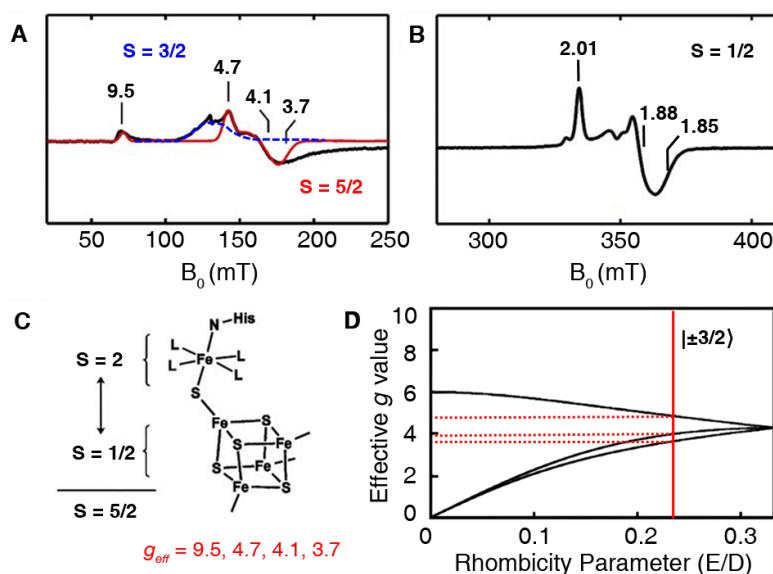

Figure 12. EPR spectroscopic characterisation of the [5Fe-5S] cluster in the assembly of [FeFe]-hydrogenases. (A) Low-field region of the X-band CW EPR spectrum (10K) showing evidence of a high-spin [5Fe-5S] cluster with spin S = 5/2 (simulation in red) and 3/2 (simulation in blue). (B) High-field region showing the [4Fe-4S] S = 1/2 cluster. (C) Exchange coupling scheme for the formation of the S = 5/2 [5Fe-5S] cluster. (D) Partial rhombogram for S = 5/2, showing effective g values for the m_S = ±3/2 intradoublet transitions when E/D = 0.225 (±1/2 and ±5/2 intradoublet transitions not shown). Adapted from [4,44].

---

[4] Note that the other two g values are not observed because these are << 1.

5.2   Light induced phenomena

Time-resolved EPR (TREPR) enables the investigation of light-induced events such as photo-redox reactions, formation of photoexcited triplet states and radical pairs,[45] and homolytic dissociation of chemical bonds. A laser flash generates the paramagnetic species (e.g. triplet or radical) and pulsed EPR experiments (i.e. detecting the electron spin echo, see Box 10) in the excited state can be performed as well as CW EPR. In this section, we provide an introduction to triplet-state EPR spectra and discuss examples. For further literature in the field, the reader is referred to ref. [46].

5.2.1   Introduction to triplet-state EPR spectra

Let us consider a chromophore in its ground singlet state with an allowed optical absorption. Upon absorption of a photon, the chromophore is excited to its first excited singlet state. This can either decay back to the ground state (fluorescence or non-radiative decay) or cross to a triplet state via the intersystem crossing (ISC) mechanism. Triplet states are characterised by two unpaired electrons with parallel spins (S = 1) with three corresponding triplet sublevels X, Y, Z. The triplet sublevels are labelled as X, Y, Z in zero field and as 0, ±1 in high field, since the m_S quantum number is meaningful only at high field (Figure 13A, C). Since ISC is an anisotropic process, the transitions from the singlet excited state to the three triplet sublevels (and the decay rates from the three triplet sublevels to the ground singlet state) generally have different probabilities as determined by the molecular symmetry. Consequently, the populations of the triplet sublevels do not follow the Boltzmann distribution and are said to be *spin polarised*. Moreover, even in the absence of an applied field the energies of the triplet sublevels are usually non-degenerate and the relative splittings depend on the ZFS parameters (Section 2.6), as sketched in Figure 13B. The corresponding transitions can be probed directly in zero-field and the most common way for organic triplet states is Optically Detected Magnetic Resonance.[47]

When an external field is applied as customary in EPR, the EZ interaction also needs to be considered. Figure 13C shows the energy level diagram for the simple case of the applied magnetic field parallel to the Z sublevel, in the assumption that the EZ interaction is much larger

than all other interactions. The energy of this sublevel does not depend on the strength of the applied field, whereas the energy of the other sublevels mix and split proportionally to the applied field strength. Similar considerations apply to the spin populations (P_i): P_Z is unaffected whereas the populations of the other two sublevels in high-field are the average of the corresponding populations in zero field. Similar energy-level schemes can be drawn for the applied field parallel to the X and Y axes of the ZFS tensor.

The TREPR spectrum of a photoexcited triplet presents some distinctive characteristics. First, the EPR spectrum features two allowed ($\Delta m_S = \pm 1$) transitions for each molecular orientation (Figure 13C). Second, since the sublevels are spin polarised, both enhanced absorption and emission peaks are observed (Figure 13D). When the sample is isotropic and all possible orientations are present (i.e. in a powder sample or frozen solution), the resulting 'powder average' spectrum (Figure 13E) has six distinguishable turning points. From their positions, the magnitude (but not the sign) of the ZFS parameters can be derived. If $E = 0$ (i.e. X = Y) only four turning points are present.
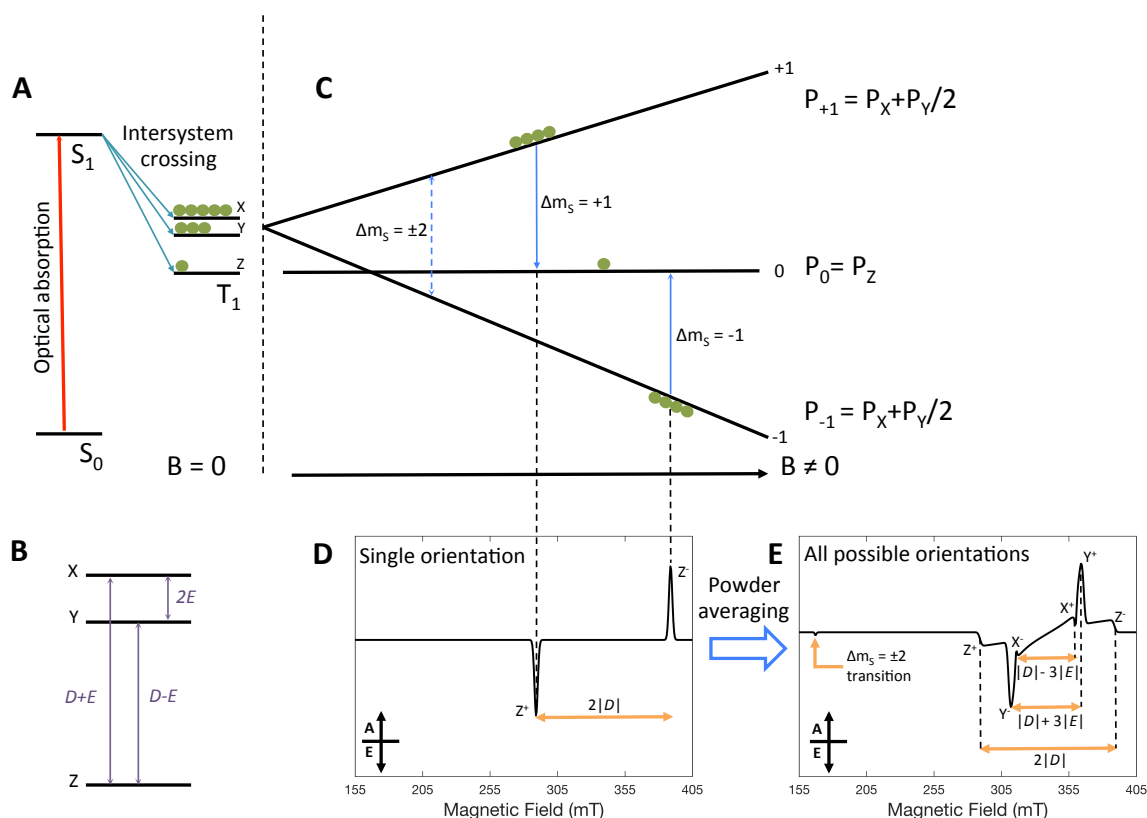
Figure 13. Illustration of the origin of triple-state EPR spectra. (A) Formation of a triplet via intersystem crossing from the first excited singlet. The populations of the three sublevels are represented with green circles and do not follow the Boltzmann distribution. (B) EPR transitions in zero field. The ordering of the energy levels depends on the sign of the ZFS parameters; in the case illustrated $D, E > 0$. (C) In presence of an applied field two allowed EPR transitions can be observed for each molecular orientation (here B_0 is parallel to the Z axis of the ZFS tensor). (D) EPR spectrum corresponding to C. (E) Simulated powder-average EPR spectrum for the isotropic case.

5.2.2   Identification of energy transfer partners (electron spin polarization)

Triplet excitation can be transferred from one site to another in a down-hill process. Photosynthetic light-harvesting complexes provide a prominent example when, under high light conditions, carotenoid triplet states are populated from chlorophyll triplet states in order to scavenge singlet oxygen. The electron spin polarisation (ESP) produced at the carotenoid acceptor site depends on the initial polarisation of the chlorophyll donor and on the relative geometrical arrangement of the donor-acceptor ZFS axes. This is because the triplet-triplet energy transfer mechanism occurs by an electron exchange mechanism with conservation of spin angular momentum. Therefore, the measured ESP at the acceptor site (i.e. spectral shape) can be exploited to distinguish between competing donor-acceptor pairs, as it was shown for the peridinin-chlorphyll *a*-protein complex where a single chlorophyll is surrounded by 4 carotenoids.[48] Figure 14 shows a comparison between the experimental TREPR spectrum for the carotenoid and those calculated for each carotenoid-chlorophyll pair, taking into account the relative orientation of the two molecules. Clearly only the carotenoid labelled 614 gives a positive match and hence is responsible for quenching the chlorophyll triplet state.
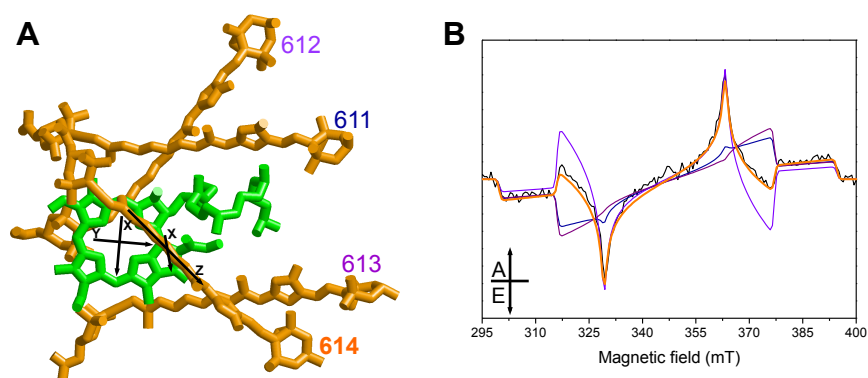
Figure 14. Electron spin polarization as a source of structural information. (A) Pigment arrangement in the peridinin-chlorphyll *a*-protein. Green= chlorophyll, orange = carotenoids. (B) Experimental TREPR spectrum of the peridinin-chlorphyll *a*-protein at 150 K (black) with the corresponding calculated EPR spectra for each carotenoid surrounding the chlorophyll donor (in colour). Only two axes for the zero-field splitting tensors (black vectors) are shown for clarity (the third is orthogonal to both). A = absorption; E = emission. Adapted from [48].

5.2.3   Molecular wires (triplet exciton delocalization)

Molecular wires, built on repeated units of π-conjugated monomers (such as porphyrins) are of interest for photonics, spintronics and molecular electronics applications. Tait et al.[49] combined TREPR (to determine zero-field splitting parameters) and ENDOR (to measure proton hyperfine couplings) spectroscopies on photoexcited porphyrin linear oligomers (up to 6 units, Figure 15A) to measure the extent of spatial delocalization of the triplet exciton.

For an evenly delocalized triplet, the ZFS parameter D resulting from the spin-spin coupling of the unpaired electrons (see Section 2.7, Box 7) was expected to decrease proportionally to the number of units (i.e. the average distance). Unexpectedly, no significant change in the zero-field splitting parameters (D and E) could be observed for linear oligomers with two to six porphyrin units (see Figure 15B for a comparison of the monomer and dimer). In contrast, the spin polarization of the triplet state EPR spectra proved to be sensitive to the number of porphyrin units, demonstrating a different probability of populating the triplet sublevels with the number of units (Figure 15B). In addition, the proton hyperfine couplings provided a highly reliable method to *quantify* the extent of the triplet delocalization: whereas delocalisation is complete in the dimer ($A_{monomer} = 2A_{dimer}$, Figure 15C), the spin density is *not* distributed evenly over the whole π-system beyond the dimer (Figure 15D). Hyperfine coupling constants can therefore reliably assess the extent of spin delocalisation. EPR spectroscopy proves a fundamental difference between excited singlet and triplets in linear porphyrin nanowires: while in the former the spin is evenly delocalised over the whole structure, in the latter it is localised over just the central porphyrin units.
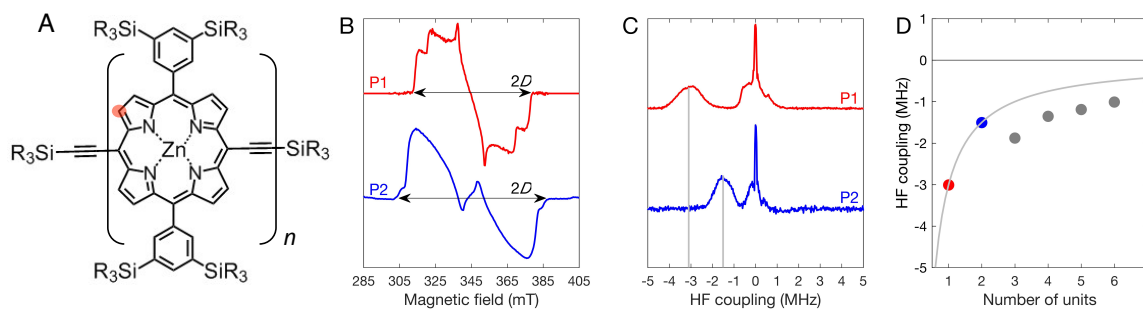
Figure 15. Triplet delocalisation in molecular wires of different lengths. (A) Molecular structure of the porphyrin moiety P where R = *n*-hexyl. (B) TREPR spectra of P1 (*n*=1) and P2 (*n*=2) at 20K. (C) ENDOR spectra showing the hyperfine coupling A of the H_1 protons (red circle in A) in excited P1 and P2. (D) Hyperfine couplings as a function of oligomer size (P1 to P6). The fitted line corresponds to the theoretical hyperfine couplings predicted for complete delocalization. Adapted with permission from [49]. Copyright 2015 American Chemical Society.

5.3   Distance measurements

Pulsed dipolar spectroscopy constitutes a set of EPR experiments that enable the measurement of dipolar couplings between electron spins – naturally occurring or engineered as spin-labels – directly. These experiments can involve a single microwave frequency, e.g. DQC (Double Quantum Coherence) and RIDME (Relaxation-Induced Dipolar Modulation Enhancement) or, in the vast majority of cases, two microwave frequencies. The latter two-microwave frequency experiment is known as DEER (Section 2.8.3), also known as PELDOR (Pulsed ELectron DOuble Resonance). Because the dipolar coupling is inversely proportional to the interspin distance cubed (Section 2.7, equation 8, Box 7), pulsed dipolar spectroscopy provides information on the distance between electron spins. The technique has been applied to synthetic and biological systems alike, but is particularly suitable for dynamic systems too flexible to be crystallised or too large to be studied by NMR, and often complements other techniques, such as small-angle X-ray scattering or cryo-electron microscopy. Pulsed dipolar spectroscopy can assess distances between 1.8 and 8 nm (in fully deuterated media up to 13 nm) and not only provides an average interspin distance but also the distance *distribution*. Thus, it enables the characterisation of conformational distributions on a nanometer scale. Porphyrin wires similar to those discussed above but labelled at both ends with stable nitroxide radicals (Figure 16A) illustrate the inverse dependence of inter-spin distance and dipolar frequency. As shown in Figure 16B, as the series progresses from one to four units (inter-spin distances 3.4 and 7.5 nm, respectively), the dipolar

frequency measured through the DEER experiment decreases from ca. 1.3 MHz to 0.1 MHz (corresponding to modulation periods of ca. 0.8 and 7 μs, respectively). The resulting distance distributions are a manifestation of the rigidity and shape-persistence of such wires in solution (Figure 16C) and indeed Figure 16D shows that the inter-spin distances derived from EPR experiments are in excellent agreement with those estimated from crystallographic data. DEER can thus be used to measure nanometer distances reliably in disordered systems such as frozen solutions.
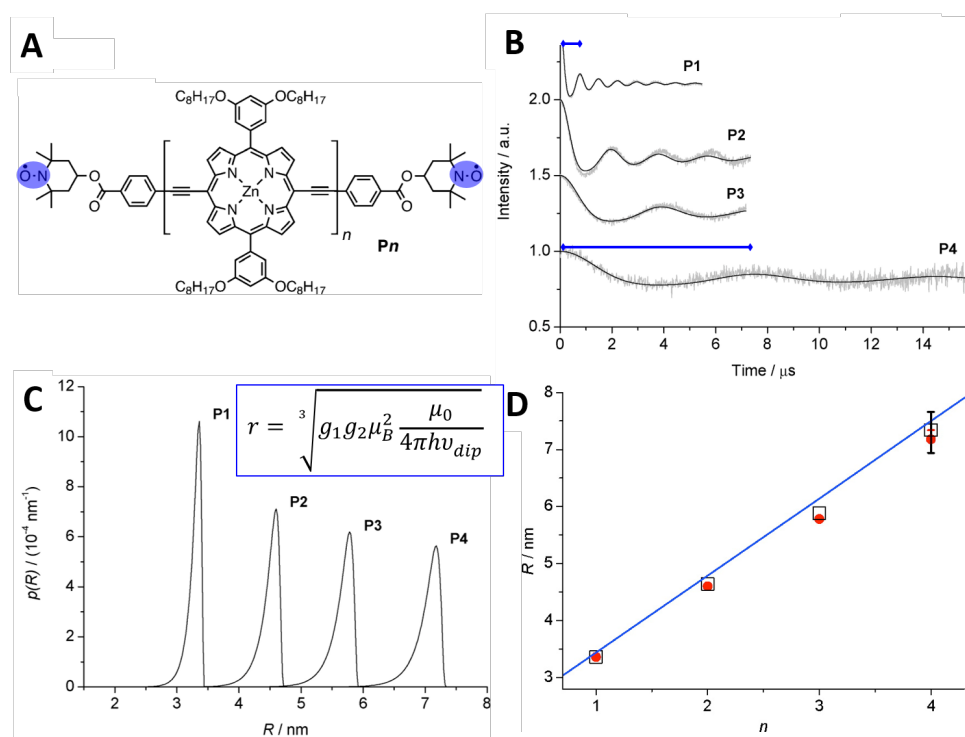

Figure 16: Determining molecular wire lengths (distances) using DEER spectroscopy. (A) Molecular structure of the porphyrin wires (Pn), with n = 1 to 4; the nitroxide moieties are highlighted in blue. (B) Experimental time traces with fits (the periods for n = 1 and n = 4 are indicated by blue horizontal bars). The modulation periods for P1 and P4 are indicated by blue bars. (C) Distance distributions with equation relating inter-spin distance (r) and measured dipolar frequency (ν_{dip}). For a pair of nitroxide radicals, with $g_1 = g_2 \approx 2.0069$, the equation can take the form $r = \sqrt[3]{52.19 \, MHz/\nu_{dip}}$ (where r is in nm) and it follows that at a dipolar frequency of $\sim$ 52 MHz corresponds a distance of $\sim$ 1 nm. (D) Comparison between DEER distances (data points) and crystallographic data (solid line). Adapted with permission from [50]. Copyright 2009 American Chemical Society.

A full description of the theory behind pulsed dipolar spectroscopy and its applications is outside the scope of this tutorial review but can be found in ref.[51] and in the recently published chapters of *eMagRes*. For a review showcasing the latest developments in spin-labelling

techniques for EPR distance measurements, with emphasis on the contribution of chemistry to the field, see ref. [52].

6   Concluding remarks

This tutorial review has highlighted some of diverse problems that can be solved using various EPR spectroscopic techniques. We hope to have provided the reader with a basic set of tools and a foundation of the physical principles to tackle the interpretation of EPR data. We have seen that CW EPR involves observing transitions *between* electron spin states. On the other hand, pulse EPR enables access to transitions *within* electron-spin states and although the entire spin system may be complicated, different experiments can conveniently single out different interactions. A key point is that simulations are often essential in order to interpret EPR spectra and obtain accurate coupling parameters. Freely available simulation programs are becoming increasingly user friendly and satisfy the demands of the beginner as well as the expert user. It is important to emphasise that EPR spectroscopy often complements other methods, such as theoretical calculations. Technological developments in EPR spectroscopy are advancing quickly. Increasingly high-frequency/high-field spectrometers are becoming commercially available, and user-friendly bench top X-band instruments are able to satisfy the needs of many users. As the field and users of EPR spectroscopy expand, many new problems in the chemical sciences will be answered and we hope that this tutorial review has sparked the curiosity of the reader to explore the fascinating world of unpaired electrons.

ABBREVIATIONS

CW = continuous wave; ν_I = Larmor frequency of a nucleus; ν_{mw} = applied microwave frequency; ENDOR = electron nuclear double resonance; ESEEM = electron spin echo envelope modulation; HYSCORE = hyperfine sublevel correlation; ZFS = zero field splitting; TREPR = time-resolved EPR; DEER = double electron-electron resonance; ISC = intersystem crossing.

BIOBLIOGRAPHY

1   V. Chechik, E. Carter and D. Murphy, *Electron paramagnetic resonance*, Oxford University Press, Oxford, 2016.

2   W. R. Hagen, *Biomolecular EPR spectroscopy*, CRC Press, Boca Raton, 2009.

3   M. Brustolon and G. Giamello, *Electron paramagnetic resonance: a practitioner's toolkit*, Wiley, New Jersey, 2009.

4   W. R. Hagen, *Dalt. Trans.*, 2006, **56**, 4415–34.

5   A. Brückner, *Chem. Soc. Rev.*, 2010, **39**, 4673–84.

6   D. M. Murphy and R. D. Farley, *Chem. Soc. Rev.*, 2006, **35**, 249–268.

7   F. A. Villamena, in *Reactive Species Detection in Biology - from Fluorescence to Electron Paramagnetic Resonance Spectroscopy*, Elsevier, Boston, 1st edn., 2017, pp. 163–202.

8   P. Kuppusamy and J. L. Zweier, *NMR Biomed.*, 2004, **17**, 226–239.

9   F. Jelezko and J. Wrachtrup, *Phys. status solidi*, 2006, **203**, 3207–3225.

10   P. Fattibene and F. Callens, *Appl. Radiat. Isot.*, 2010, **68**, 2033–2116.

11   J. A. Weil and J. R. Bolton, *Electron paramagnetic resonance : elementary theory and practical applications.*, Wiley, New Jersey, 2007.

12   A. Schweiger and G. Jeschke, *Principles of pulse electron paramagnetic resonance*, Oxford University Press, Oxford, 2001.

13   C. P. Poole, *Electron spin resonance : a comprehensive treatise on experimental techniques*,

Dover Publications, New York, 1996.

14   *eMagRes*, John Wiley & Sons, 2017.

15   N. Le Breton, J. J. Wright, A. J. Y. Jones, E. Salvadori, H. R. Bridges, J. Hirst and M. M. Roessler, *J. Am. Chem. Soc.*, 2017, **139**, 16319–16326.

16   D. Goldfarb, *Phys. Chem. Chem. Phys.*, 2006, **8**, 2325–2343.

17   S. Stoll and D. Goldfarb, in *eMagRes*, John Wiley & Sons, Ltd, 2007.

18   A. T. Taguchi, P. J. O'Malley, C. A. Wraight and S. A. Dikanov, *J. Phys. Chem. B*, 2014, **118**, 1501–1509.

19   C. Duboc, *Chem. Soc. Rev.*, 2016, **45**, 5834–5847.

20   G. R. Eaton and S. S. Eaton, in *Multifrequency Electron Paramagnetic Resonance: Theory and Applications*, ed. S. K. Misra, Wiley-VCH, New Jersey, 2011, pp. 719–753.

21   S. S. Eaton and G. R. Eaton, in *Biological Magnetic Resonance, Volume 19: Distance Measurements in Biological Systems by EPR*, eds. L. J. Berliner, S. S. Eaton and G. R. Eaton, Kluwer Academic Publishers-Plenum Publishers, New York, 2000, pp. 29–154.

22   G. Jeschke, in *ESR Spectroscopy in Membrane Biophysics*, eds. L. Hemminga and L. Berliner, Springer US, Boston, 2007, pp. 17–47.

23   J. Harmer, G. Mitrikas and A. Schweiger, in *High Resolution EPR*, eds. L. Berliner and G. Hanson, Springer, New York, 2009, pp. 13–61.

24   S. Stoll and A. Schweiger, *J. Magn. Reson.*, 2006, **178**, 42–55.

25   S. Stoll and R. D. Britt, *Phys. Chem. Chem. Phys.*, 2009, **11**, 6614–6625.

26   H. J. Hogben, M. Krzystyniak, G. T. P. Charnock, P. J. Hore and I. Kuprov, *J. Magn. Reson.*, 2011, **208**, 179–194.

27   A. Okafuji, A. Schnegg, E. Schleicher, K. Möbius and S. Weber, *J. Phys. Chem. B*, 2008, **112**, 3568–3574.

28   F. Neese, in *Multifrequency Electron Paramagnetic Resonance*, Wiley-VCH Verlag GmbH & Co. KGaA, 2011, pp. 295–326.

29   E. Morra, S. Maurelli, M. Chiesa and S. Van Doorslaer, *Phys. Chem. Chem. Phys.*, 2015, **17**, 20853–20860.

30   N. K. Solanki, E. J. L. McInnes, F. E. Mabbs, S. Radojevic, M. McPartlin, N. Feeder, J. E. Davies and M. A. Halcrow, *Angew. Chemie Int. Ed.*, 1998, **37**, 2221–2223.

31   J. M. Holland, X. Liu, J. P. Zhao, F. E. Mabbs, C. A. Kilner, M. Thornton-Pett and M. A. Halcrow, *J. Chem. Soc. Dalt. Trans.*, 2000, **19**, 3316–3324.

32   J. F. Gibson, D. O. Hall, J. H. Thornley and F. R. Whatley, *Proc. Natl. Acad. Sci. U. S. A.*, 1966, **56**, 987–990.

33   R. Malkin and A. J. Bearden, *Proc. Natl. Acad. Sci. U. S. A.*, 1971, **68**, 16–19.

34   S. Stoll, H. S. Shafaat, J. Krzystek, A. Ozarowski, M. J. Tauber, J. E. Kim and R. D. Britt, *J. Am. Chem. Soc.*, 2011, **133**, 18098–18101.

35   C. J. Adams, R. B. Bedford, E. Carter, N. J. Gower, M. F. Haddow, J. N. Harvey, M. Huwe, M. Á. Cartes, S. M. Mansell, C. Mendoza, D. M. Murphy, E. C. Neeve and J. Nunn, *J. Am. Chem. Soc.*, 2012, **134**, 10333–10336.

36   A. Zoleo, R. G. Lawler, X. Lei, Y. Li, Y. Murata, K. Komatsu, M. Di Valentin, M. Ruzzi and N. J. Turro, *J. Am. Chem. Soc.*, 2012, **134**, 12881–12884.

37   T. Spatzal, M. Aksoyoglu, L. Zhang, S. L. A. Andrade, E. Schleicher, S. Weber, D. C. Rees and O. Einsle, *Science (80-.).*, 2011, **334**, 940–940.

38   C. J. Fugate, T. A. Stich, E. G. Kim, W. K. Myers, R. D. Britt and J. T. Jarrett, *J. Am. Chem. Soc.*, 2012, **134**, 9042–9045.

39   W. Wang, J. Li, K. Wang, T. I. Smirnova and E. Oldfield, *J. Am. Chem. Soc.*, 2011, **133**, 6525–6528.

40   M. M. Roessler, R. M. Evans, R. A. Davies, J. Harmer and F. A. Armstrong, *J. Am. Chem. Soc.*, 2012, **134**, 15581–15594.

41   S. Grimaldi, R. Arias-Cartin, P. Lanciano, S. Lyubenova, B. Endeward, T. F. Prisner, A. Magalon and B. Guigliarelli, *J. Biol. Chem.* , 2010, **285**, 179–187.

42   J. Krzystek, A. Ozarowski, J. Telser and D. C. Crans, *Coord. Chem. Rev.*, 2015, **301**, 123–133.

43   J. Ferrando-Soria, E. Moreno Pineda, A. Chiesa, A. Fernandez, S. A. Magee, S. Carretta, P. Santini, I. J. Vitorica-Yrezabal, F. Tuna, G. A. Timco, E. J. L. McInnes and R. E. P. Winpenny, *Nat. Commun.*, 2016, **7**, 11377.

44   P. Dinis, D. L. M. Suess, S. J. Fox, J. E. Harmer, R. C. Driesener, L. De La Paz, J. R. Swartz, J. W. Essex, R. D. Britt and P. L. Roach, *Proc. Natl. Acad. Sci. U. S. A.*, 2015, **112**, 1362–7.

45   W. Lubitz, F. Lendzian and R. Bittl, *Acc. Chem. Res.*, 2002, **35**, 313–320.

46   N. Hirota and S. Yamauchi, *J. Photochem. Photobiol. C Photochem. Rev.*, 2003, **4**, 109–124.

47   D. Carbonera, *Photosynth. Res.*, 2009, **102**, 403–414.

48   M. Di Valentin, S. Ceola, E. Salvadori, G. Agostini and D. Carbonera, *Biochim. Biophys. Acta - Bioenerg.*, 2008, **1777**, 186–195.

49   C. E. Tait, P. Neuhaus, M. D. Peeks, H. L. Anderson and C. R. Timmel, *J. Am. Chem. Soc.*, 2015, **137**, 8284–8293.

50   J. E. Lovett, M. Hoffmann, A. Cnossen, A. T. J. Shutter, H. J. Hogben, John E Warren, Sofia I Pascu, C. W. M. Kay, C. R. Timmel and H. L. Anderson, *J. Am. Chem. Soc.*, 2009, **131**, 13852–13859.

51   G. Jeschke, *Annu. Rev. Phys. Chem.*, 2012, **63**, 419–446.

52   A. Fielding, M. Concilio, G. Heaven and M. Hollas, *Molecules*, 2014, **19**, 16998–17025.